End of study project

# Estimation of biodiversity variables of a Mediterranean forest for two French and American hyperspectral space missions (CNES and NASA)

*Supervisors :*
Karine Adeline (ONERA)
Jean-Philippe Gastellu-Etchegorry (CESBIO)
Xavier Briottet (ONERA)
Thomas Miraglio (ONERA)
José Radzik (ISAE)
Jérôme Lacan (ISAE)

*Author :*
Louis Chauvet

Version 3 of
November 21, 2020

Date: April 2020 - October 2020
Location: ONERA centre de Toulouse - 2 avenue Edouard Belin 31000 TOULOUSE

# Acknowledgments

I would first like to thank my supervisors Karine Adeline, Xavier Briottet, Jean-Philippe Gastellu-Etchegorry, Thomas Miraglio and José Radzik who, despite the context, were able to remain available, attentive and full of valuable advice for the entire internship.

I would also like to thank the ONERA for welcoming me in their premises and the members of the DOTA department for the good working atmosphere and the good laughs we had.

I am grateful for IMT Atlantique and ISAE Supaero which opened up many possible paths to me including the one leading to this end-of-studies internship.

Finally, I would like to thank Valentin Breton for his relevant observations and his expertise.

# Contents

**Acknowledgments** **i**

**Contents** **ii**

**List of Figures** **iv**

**List of Tables** **vi**

**List of abbreviations and acronyms** **vii**

**Introduction** **1**

**1 Working environment** **3**

1.1 CESBIO . . . 3

1.2 ONERA . . . 3

1.2.1 ONERA's structure . . . 4

1.2.2 DOTA . . . 4

**2 Scientific context and objectives** **5**

2.1 Scientific context . . . 5

2.2 Objectives . . . 7

**3 Materials and Methods** **8**

3.1 Materials . . . 8

3.1.1 SJER study site . . . 8

3.1.2 Field data . . . 9

3.2 General Methodology . . . 13

3.2.1 Image processing . . . 14

3.2.2 Classification map using supervised vector machine . . . 17

3.2.3 DART software . . . 18

3.2.4 LUT-based inversion strategies . . . 22

**4 Results** **26**

4.1 Classification map . . . 26

4.2 LUT-based inversion . . . 28

4.2.1 Chlorophylls a+b content ($C_{ab}$) and Carotenoids content ($C_{car}$) estimations performance . . . 29

4.2.2 Leaf Area Index (LAI) estimations performance . . . 32

4.2.3 Dry matter content ($C_m$) and Equivalent water thickness ($C_w$) estimations performance . . . . . 35
**5 Discussions** **36**
5.1 Limitations of the results on biochemical properties . . . . . 36
5.2 Results distributions on the whole SJER study site . . . . . 37
5.2.1 Distribution of canopy cover among the estimates . . . . . 37
5.2.2 Distribution of the estimates on the whole SJER study site . . . . . 38
5.3 DART parameters and convenience of the different LUTs for the inversion . 42
5.4 HYPXIM (8 m) and SBG (30 m) spatial resolutions performances . . . . . 43
**Conclusion and prospects** **44**
**Bibliography** **45**
**Appendices** **48**
**Abstract** **54**

# List of Figures


2.1 Absorption spectra of foliar pigments . . . . . 6

3.1 Dominant tree species of SJER . . . . . 8
3.2 Location of the SJER study site in California . . . . . 9
3.3 Airborne images of the SJER study site summer 2014 working zone . . . . 10
3.4 Examples of measurements for background spectra . . . . . 11
3.5 SJER QUDO trunk reflectance spectrum . . . . . 11
3.6 Digital hemispherical photography acquisitions . . . . . 12
3.7 Methodology followed for the internship . . . . . 13
3.8 Result of image co-registration between AV-C and AV-NG . . . . . 14
3.9 Simulations images up to 30m . . . . . 15
3.10 MCARI2 masking of the AV-NG 2.1 m image . . . . . 16
3.11 Spectra of the training dataset of the SVM classifier . . . . . 17
3.12 SJER scene for CC 50 % in DART . . . . . 19
3.13 Resulting image of one DART simulation and pixels selection for the LUT 21
3.14 Reflectance spectra for both LUTs.Both spectra registered in the LUTs entry for $CC = 50\%$, LAI = 1.9, $C_{ab} = 30$ µg/cm$^2$, $C_{car} = 14$ µg/cm$^2$, $C_w = 0.016$ g/cm$^2$, $C_m = 0.013$ cm. . . . . 22
3.15 Example of VIs variation within the LUT cases . . . . . 24

4.1 Confusion matrix of the SVM classifier . . . . . 26
4.2 Classification map of the AV-NG 2.1 m image using SVM . . . . . 27
4.3 Reflectances computed by the DART simulations compared to reflectances of vegetation pixels within the AV-NG and AV-C image . . . . . 28
4.4 Biophysical-chemical measurements location . . . . . 29
4.5 Measured versus estimated leaf $C_{car}$ using $D_{CRI}$ and $D_{\rho_{515}/\rho_{570}}$ methods . . 30
4.6 Measured versus estimated leaf $C_{ab}$ using $D_{GM_94b}$ and $D_{gNDVI}$ methods . 31
4.7 Measured versus estimated plot LAI using RMSE INT LAI and $D_{MSAVI2}$ methods . . . . . 33
4.8 LAI estimation on SJER study site at 31.5 m spatial resolution . . . . . 34

4.9 Measured versus estimated leaf $C_m$ using $D_{NDNI}$ and $C_w$ using $D_{SRWI}$ methods 35

5.1 Canopy cover distribution among the estimates for the inversion strategies considered . . . . . 38
5.2 $C_{ab}$ inversion maps distributions . . . . . 39
5.3 $C_{car}$ inversion maps distributions . . . . . 40
5.4 $C_{ab}$ inversion map at 2.1 m using $D_{GM_94b}$ and SAM INT CAB . . . . . 41
5.5 Pixel selections for the different LUTs . . . . . 42
A.1 VIs variation function of $C_{ab}$ . . . . . 48
A.2 VIs variation function of $C_{car}$ . . . . . 49
A.3 VIs variation function of LAI . . . . . 50

# List of Tables


3.1 Biochemistry and LAI measured on site during Summer 2014 . . . . . 13

3.2 QUDO tree inventory campaigns overview (5 campaigns between 2013 and 2015) . . . . . 19

3.3 DART inputs for the scene modeling . . . . . 20

3.4 DART vegetation input parameters for the LUT . . . . . 21

3.5 Spectral strategies applied for the inverse problem . . . . . 25

4.1 $C_{ab}$ and $C_{car}$ retrieval performance with the standard LUT . . . . . 30

4.2 $C_{ab}$ and $C_{car}$ retrieval performance with the tree centered pixels LUT . . . 31

4.3 LAI retrieval performance with the standard LUT . . . . . 33

4.4 $C_m$ and $C_w$ retrieval performance with the standard LUT . . . . . 35

A.1 Variable retrieval performances for the standard LUT results . . . . . 51

A.2 Variable retrieval performances for the tree centered pixels LUT . . . . . 52

# List of abbreviations and acronyms

| | |
|---|---|
| **AV-C** | AVIRIS-Classic |
| **AV-NG** | AVIRIS-Next-Generation |
| **BRF** | Bidirectional Reflectance Factor |
| $C_{ab}$ | Chlorophylls a+b content |
| $C_{car}$ | Carotenoids content |
| **CC** | Canopy Cover |
| $C_m$ | Dry matter content |
| $C_w$ | Equivalent water thickness |
| **CESBIO** | Centre d'Etudes Spatiales de la BIOsphère |
| **CNES** | Centre National d'Etudes Spatiales |
| **DART** | Discrete Anisotropic Radiative Transfer |
| **DGA** | Direction Générale de l'Armement |
| **DHP** | Digital Hemispherical Photography |
| **DOTA** | Département Optique et Techniques Associées |
| **EBV** | Essential Biodiversity Variable |
| **EPIC** | Etablissement public à caractère industriel et commercial |
| **ESA** | European Space Agency |
| **FIR** | Far Infrared |
| **ICOS** | Integrated Carbon Observation System |
| **INSU** | Institut National des Sciences de l'Univers |
| **LAI** | Leaf Area Index |
| **LUT** | LookUp Table |
| **NIR** | Near InfraRed |
| **ONERA** | Office National d'Etudes et de Recherches Aérospatiales |
| **OSR** | Observatoire Spatial Regional |
| **PAI** | Plant Area Index |
| **PISA** | Pinus Sabiniana |
| **QUDO** | Quercus douglasii |
| **QUWI** | Quercus wislizeni |
| **RMSE** | Root-Mean-Square Error |
| **SAM** | Spectral Angle Mapper |
| **SJER** | San Joaquin Experimental Range |
| **SME** | Small and Medium Enterprise |
| **SNR** | Signal to Noise Ratio |
| **SVM** | Support Vector Machine |
| **SWIR** | Short Wave Infrared |
| **TIR** | Thermal InfraRed |
| **TONZI** | Tonzi Ranch |
| **UV** | UltraViolet |
| **VI** | Vegetation Index |
| **VIS** | VISible domain |

# Introduction

The significant degradation of the vegetation biodiversity in recent decades has led ecologists to define Essential Biodiversity Variables (EBVs) to characterize it. They are determined at several scales: ecosystem, population and individual. Remote sensing allows the monitoring of some EBVs over large areas such as those characterizing tree species at the population scale (abundance, richness, distribution) and the evaluation of functional characteristics for each species, including their biophysical and biochemical properties. These are relevant indicators of plant functioning, affecting their productivity and ecosystem functions. The most studied biochemical properties by remote sensing are leaf pigments (chlorophylls and carotenoids), water content and dry matter content, which are involved respectively in the phenological cycle of the plant, its water stress and its biomass. Among the biophysical properties, the one most commonly studied is the Leaf Area Index (LAI).

The goal of this internship is to assess and compare the performance of future French and American satellite missions, HYPXIM / BIODIVERSITY and SBG respectively, to develop a mapping of the biophysical-chemical properties of trees in Mediterranean forests in order to be able to monitor their state of health over time, particularly in the context of drought.

The wooded savanna site studied, San Joaquin Experimental Range (SJER), is located in the Sierra Nevada in California, on which several field measurement campaigns were carried out [1], complemented by an airborne hyperspectral acquisition AVIRIS-Next-Generation (AV-NG) at 2 m spatial resolution and AVIRIS-Classic (AV-C) at 18 m.

This internship, financed by the Centre d'Etudes Spatiales de la BIOsphère (CESBIO) and taking place on the premises of the Office National d'Etudes et de Recherches Aérospatiales (ONERA) in Toulouse, is part of the APR Centre National d'Etudes Spatiales (CNES) HyperMED project - "Evaluation of the functional characteristics of tree species for monitoring their state of health in Mediterranean forest ecosystems for a hyperspectral imager" and in support of Thomas Miraglio's thesis [2, 3]. This work is done in collaboration with S. Ustin and M. Huesca from CSTARS, University of Davis, California, USA.

This report first details the framework in which the internship was carried out. Then it describes the path followed and the methodology used to obtain EBV estimates from remote sensing data using a combination of image processing and a radiative transfer tool to perform a LookUp Table (LUT)-based inversion method. The results obtained are given and discussed in order to assess the performance of the different methods used and the future work considered.

# Pandemic situation

Due to the evolution of the health crisis in France at the beginning of 2020 because of the COVID-19 pandemic linked to the SARS-CoV-2 coronavirus, the French government decided to quarantine the country from March 17, 2020 to May 11, 2020. The ONERA therefore adapted its working conditions and the internship was able to start on time with teleworking until the beginning of June, when the work was then divided into 3 days per week on the Toulouse site and 2 days of teleworking.

# Chapter 1
# Working environment

## 1.1 CESBIO

The CESBIO is a research laboratory aiming to develop knowledge on the functioning of the continental biosphere at different spatial and temporal scales by making extensive use of spatial remote sensing. This knowledge enables it to propose new space missions of Earth observation. It is attached to the Université Paul-Sabatier of Toulouse. CESBIO's research work has a dual methodological and thematic purpose.

This work feeds into thematic research on the functioning of continental surfaces and interfaces (agrosystems, forest, natural and urban ecosystems, water and carbon cycles, climate change...). This research is carried out on geographical sites (South-West of France and abroad: Morocco, Tunisia, Lebanon, India, Viet Nam), where specialists from different fields meet to raise new scientific questions and where CESBIO maintains partnerships with land managers.

The information acquired by CESBIO and its partners on its various projects is capitalized in an Environmental Information System and feeds the Observatoire Spatial Regional (OSR). The OSR is a National Information System approved by the Institut National des Sciences de l'Univers (INSU) since 2007 and is currently deployed in agricultural basins near Toulouse and Marrakech. It provides a calibration and validation base for space missions and for information extraction algorithms, and an experimental field for conducting thematic research on instrumented sites. Part of the OSR Sud-Ouest's measurements contribute to the Integrated Carbon Observation System (ICOS) network. By becoming in 2017 a member of the PYGAR (Pyrénées Garonne) Workshop Area, the CESBIO has made the resources of the OSR available to a wider scientific community.

## 1.2 ONERA

The ONERA is a French public establishment of an industrial and commercial nature (Etablissement public à caractère industriel et commercial (EPIC)) under the responsibility of the Ministry of Defense. The ONERA budget amounts to 237 million euros in 2019, 55% of which is financed by contracts with industrial companies with growing orders in France and abroad [4]. The aim of ONERA is to promote and guide research and innovation in the aerospace field, in France and Europe.

### 1.2.1 ONERA's structure

ONERA's scientific pole covers the following five scientific fields: materials and structures, fluid mechanics and energy, physics, advanced numerical simulation and information processing and systems. These disciplinary fields are divided into six departments (DEMR, DMAS, DMPE, Département Optique et Techniques Associées (DOTA), DPHY, DTIS).

ONERA's partners include the main actors in the aerospace industry, such as Airbus, Safran, Thalès and Dassault Aviation for the private sector, as well as the CNES, the European Space Agency (ESA) and the Direction Générale de l'Armement (DGA) for the public sector.

ONERA has a staff of 1968, including 1504 engineers and managers, 298 PhD students, 25 post-doctoral students and 223 trainees for a total proportion of 25% of women. Last year, ONERA published 243 papers in refereed journals, 315 papers in refereed conferences. Internally it also published 1068 technical reports, 87 defended theses and 12 habilitations to conduct research (HDR) and 102 HDR doctors.

### 1.2.2 DOTA

The DOTA's mission is to carry out studies and research related to the use of the optical domain (electromagnetic waves between medium ultraviolet (200 nm) and the THz domain (1 THz $\sim$ 300 µm)), primarily for the benefit of the Aeronautics, Space and Defense domain, but also for other domains such as security, environment, astronomy, and medical imaging.

The DOTA relies on the world of university and institutional research. For a large part of its activity, it acts as a state expert. It maintains regular relations with the major industrialists in the sector and has forged links with a number of Small and Medium Enterprises (SMEs) and mid-caps through which it promotes its work. It is made up of eight research units spread over four ONERA sites.

# Chapter 2

# Scientific context and objectives

## 2.1 Scientific context

From remote sensing data, the estimation of the EBVs requires a high spectral richness in the optical domain 0.4-2.5 µm (including biochemical properties) and a spatial resolution adapted to the scale of study. The future hyperspectral Earth observation satellite missions are expected to use sensors working either at 30 m spatial resolution with a high Signal to Noise Ratio (SNR) (PRISMA, EnMAP, SBG) and at 8 m with a lower SNR (HYPXIM/BIODIVERSITY). For a resolution of 8 m, the studies can be conducted at the individual/population scales (1 to 2 trees in a pixel), whereas for a resolution of 30 m, only the population scale can be considered (several trees in a pixel). For wooded savanna ecosystems (scattered woodlands), the estimation of biophysical and chemical properties will be sensitive in the first case to the characteristics of the individuals making up the plant cover, particularly the structure of the trees (low LAI, high presence of woody elements, crown form) whereas in the second case, the general characteristics of the ecosystem will be added (low wood cover and soil impact).

Chlorophyll a is the main factor in photosynthesis while chlorophyll b plays a secondary function, supporting chlorophyll a in light absorption. The role of carotenoids is to protect chlorophyll from photo-oxidation and thylakoid membranes from destruction resulting from excess sun radiation. Quantity of carotenoids increases with plant senescence. Figure 2.1 shows the absorption spectra of these foliar pigments in the VISible domain (VIS), both have no absorption beyond 0.71 µm. Chlorophyll a and chlorophyll b will be estimated together into one variable $C_{ab}$.

The LAI describes the plant canopies, it is a dimensionless quantity ($m^2/m^2$) which is here defined by the ratio of the total superior area of the canopy's leaves over the total projected area of the canopy. The LAI is directly related to the amount of light that can be intercepted by plants. It is an important variable used to predict photosynthetic primary production, the LAI of a forest is usually around 5 or 6 [5] but the SJER study site has a lower average LAI (around 1).

The estimation of these properties for this study is based on the use of a radiative transfer tool Discrete Anisotropic Radiative Transfer (DART) [6] and LUT based inversion method [7]. DART allows to simulate the reflectance of the canopy (simulating the spectrum of a pixel of a remote sensing image) from 3D models of the tree and its structural and biochemical characteristics, taking into account the contributions of the soil and the

illumination conditions. A database (corresponding to simulated canopy reflectances) is generated from the variation of the parameters of interest to be estimated. The LUT-based inversion consists in finding the best match between this database and the measured reflectance (coming from the remote sensing image) in order to go back to the estimation of the biochemical properties.

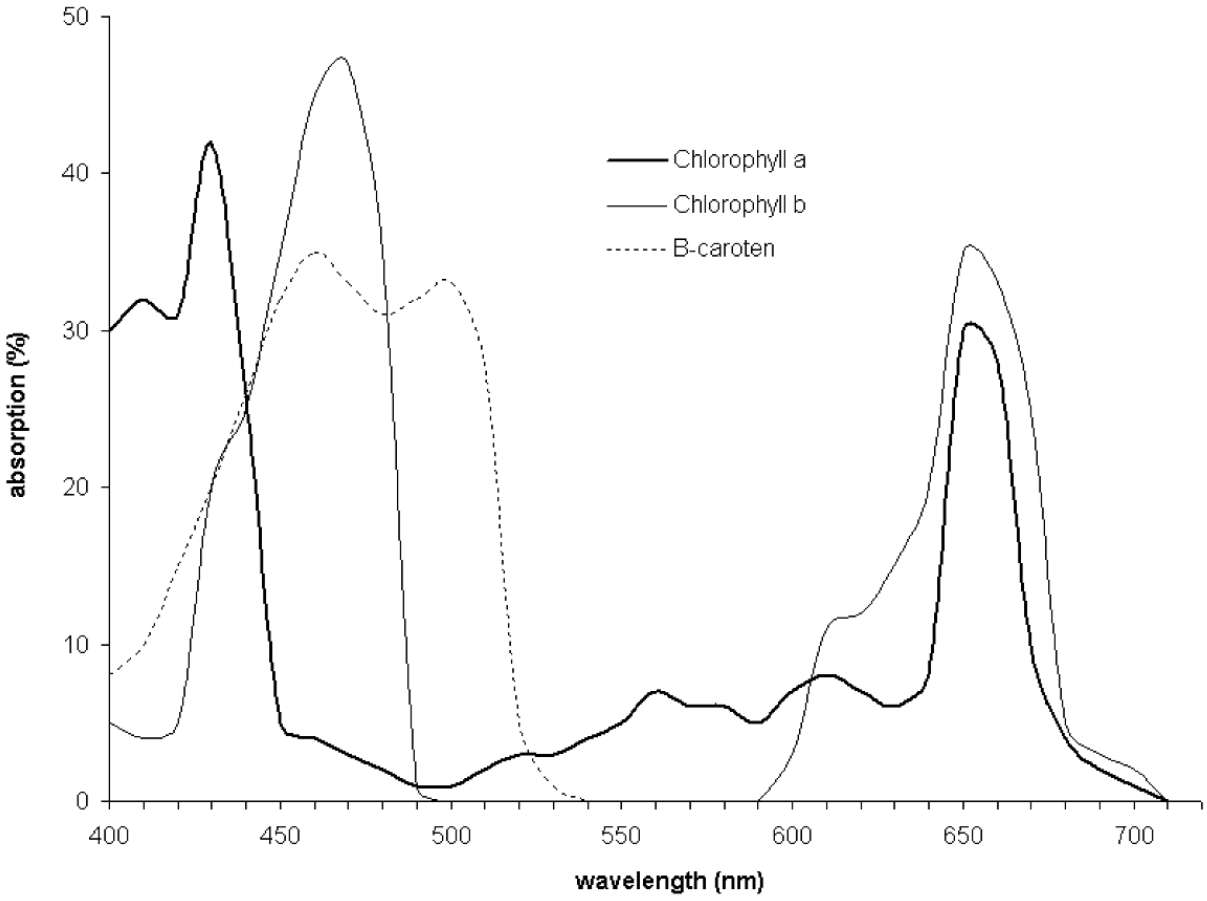


**Figure 2.1:** Absorption spectra of foliar pigments [8]
. Chlorophyll a and b will be estimated together, $C_{ab}$

## 2.2 Objectives

The internship work is mainly in support of Thomas Miraglio's work [2], trying to adapt and apply his methodology of biophysical-chemical properties estimations on another Mediterranean forest and investigating the sensitivity of the estimates to spatial resolutions and DART models. This study attempts to estimate the biochemical properties of broad-leaved trees using the same tools developped for Miraglio's PhD while developing new ones.

The internship is initially focused on the simulation of synthetic satellite images HYPXIM/BIODIVERSITY and SBG from airborne images at different spatial resolutions (ranging from 8.4 m to 31.5 m). Then on the generation of a simple simulation with DART whose 3D modeling strategy of the scene will differ according to the spatial resolution to finally arrive at the application of inversion to retrieve the biophysical-chemical properties.

# Chapter 3

# Materials and Methods

## 3.1 Materials

### 3.1.1 SJER study site

SJER is a research experimental area in the western foothills of the Sierra Nevada. The range is based in O'Neals, California, about 30 kilometres north of Fresno, California, as seen in Figure 3.2.

Within its area of roughly 1875 ha, blue oaks (Quercus douglasii (QUDO)), interior live oaks (Quercus wislizeni (QUWI)) and gray pines (Pinus Sabiniana (PISA)) are the main composition of its sparse woodland overstory. QUDOs are deciduous trees, implying that they loose their leaves at the end of their growing session (in fall for this species). In contrast QUWIs are evergreen oaks, meaning that they have green leaves throughout the year. PISAs are conifers that are particularly well adapted to growth in hot, dry climate. Pictures of a QUDO, a QUWI and a PISA are shown on Figure 3.1.
The understory is composed of scattered shrubs (mainly ceanothus and manzanita) and some annuals herbaceous plants including grasses (pine bluegrass). The soil is mainly granitic and formed in material weathered from granitic rocks. The grass and oaks trees are mainly active during the wet period (from December to May).
The climate is typical of Mediterranean climates and consists in hot, dry summers and cold, wet winters.

**(a)** Blue oak (QUDO) **(b)** Interior live oak (QUWI) **(c)** Gray pine (PISA)

**Figure 3.1:** Dominant tree species of SJER

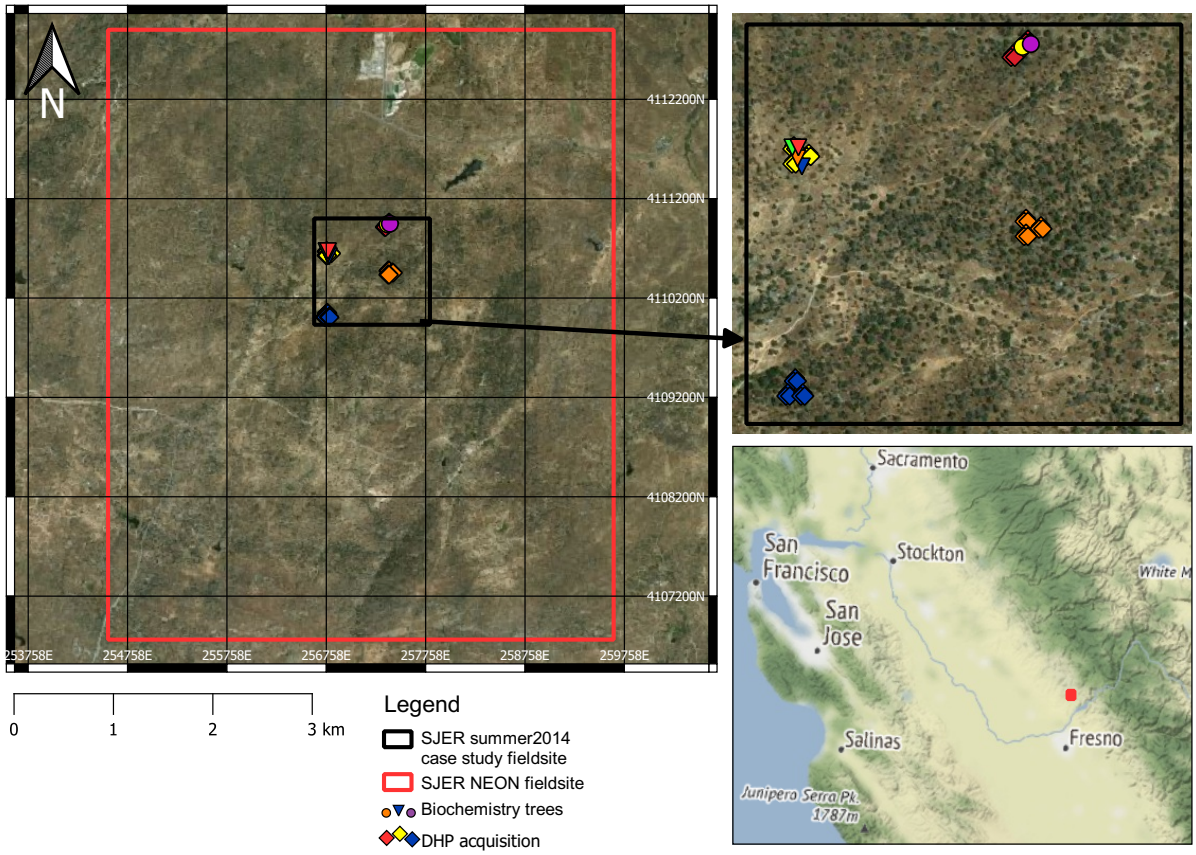


**Figure 3.2:** Location of the SJER study site in California (bottom right) and location of field measurements. Diamonds: LAI measured with DHP; colors indicate plot ID. Discs: QUWIs where leaves were sampled for laboratory biochemistry analysis. Triangles: QUDOs where leaves were sampled for laboratory biochemistry analysis; colors indicate tree ID.

### 3.1.2 Field data

#### Airborne images

The hyperspectral images used during this internship come from flight campaigns as part of the HyspIRI Preparatory Airborne Campaigns (NASA) missions that took place from 2013 to 2017 and particularly in early summer 2014 (images and information can be found on their website: https://hyspiri.jpl.nasa.gov/).

The work of this internship covers the early summer of 2014, the images were taken by two instruments. The first was taken by AVIRIS (later named AV-C), developed at Jet Propulsion Laboratory, with a whiskbroom scanner, 224 spectral bands ranging from 0.4 µm to 2.5 µm with a bandwidth of 0.01 µm and a 18 m ground sample distance [9].

The second was taken by the AVIRIS-Next-Generation instrument with 432 spectral bands ranging from 0.38 µm to 2.51 µm and ground sample distances of 2.1 m and 4.1 m. Both aerial shots were taken at nadir, AV-C was aboard an ER-2 aircraft over SJER on June 3, 2014 at an altitude of 20 km between 1:16 PM and 1:31 PM local time. Images delivered by AV-NG were taken on June 11, 2014 at an altitude of 4 km between 2:29 PM and 2:34 PM local time. Both images underwent pre-processing (radiometric calibration, geometric orthorectification, atmospheric correction, ...) in order to recover the ground reflectance by NASA JPL. Both images used for the internship are displayed on Figure 3.3.

**(a)** AVIRIS-Next-Generation 2.1 m **(b)** AVIRIS-Classic 18 m

**Figure 3.3:** Airborne images of the SJER study site summer 2014 working zone

### Leaf biochemistry

Several grounds measurements campaigns in support of the Airborne Campaigns were done from 2013 to 2017. Only data gathered during the summer of 2014 was used for this work. A collection of leaves were gathered from the higher, sunlit portion of the canopy from four different QUDOs and two QUWIs. Sampling was done the same day as the AV-NG overflight, on June 11, 2014. Leaves were collected, as high as possible in the canopy, from open developed trees in complete sunshine, and from branches on the tree's east and west sides. Leaves were then wrapped in foil packages so that they would not receive sunlight, deposited in a refrigerated container and moved to the lab refrigerator to be weighed no later than 48 hours after data collection. The leaves then went through several stages of treatment and extraction in a solution of acetone in order to measure the absorbance at specific wavelengths to calculate the concentrations of chlorophyll and carotenoids in the solutions and then finally on the leaf surface [10, 11]. Values measured are given in Table 3.1.

### Background spectra

Other measurements than leaf biochemistry were made during these ground measurements campaigns, a cover inventory was done and some elements (barks, rocks or other types of ground) were measured with a spectrometer which were used to have background spectra. Photos of various measured elements are shown on Figure 3.4.

**(a)** QUDO bark **(b)** Senescent grass **(c)** Various rocks

**Figure 3.4:** Examples of measurements for background spectra

Trunk reflectances of QUDO trees were collected on the field from 0.35 µm to 2.5 µm using an Analytical Spectral Devices, ASD Inc., Boulder, CO, USA contact probe. Figure 3.5 shows the results of these measurements. Atmospheric water absorption bands were removed from this spectra and the future ones as they disturb the measurements at these bands and were not available on the AV-NG and AV-C instruments.

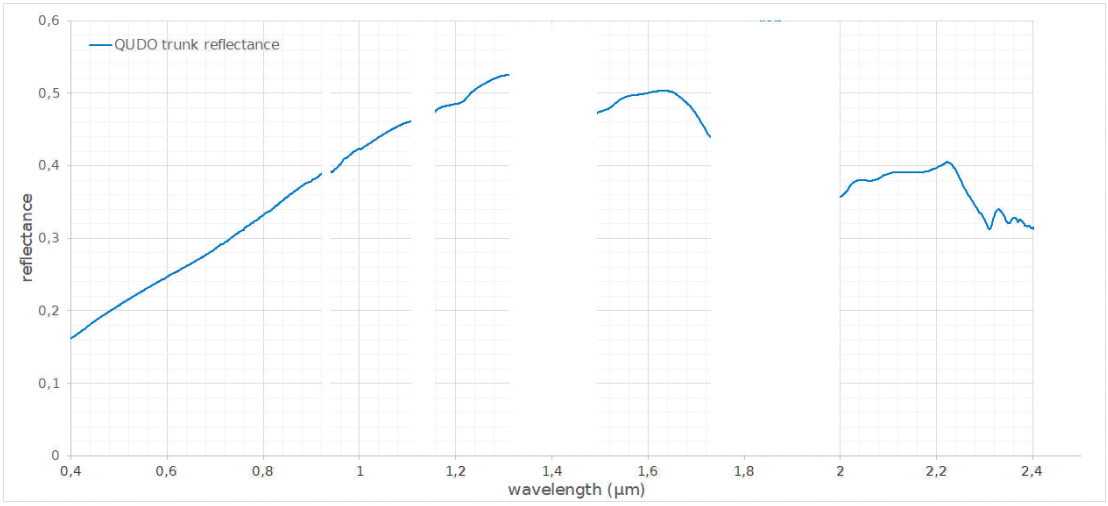


**Figure 3.5:** SJER QUDO trunk reflectance spectrum. This curve is the average of 3 measurements on QUDO trunks using an Analytical Spectral Devices, ASD Inc., Boulder, CO, USA contact probe.

### LAI computation

The LAI was measured from hemispherical photographs taken in the summer of 2014 over the whole site area mainly where the biochemical measurements were made. The photos are taken on 60 m × 60 m area divided into 9 plots (squares) of 20 m × 20 m (see Figure 3.6). Three plots were selected for each area and several pictures were taken for each plot at twilight to avoid direct sunlight on the camera lens and one of them was selected. The photographs covering different configurations of vegetation (canopy cover, tree species, ...) are processed using the CAN-EYE software (https://www6.paca.inrae.fr/can-eye) which calculates a Plant Area Index (PAI), which is similar to LAI but also counts non-photosynthetic parts of the plant, using image classification on the hemispherical photograph to classify pixels between light sky and darker vegetation. For this study we considered that the PAI of the plots were almost identical to LAI because the presence of woody elements increasing PAI with regards to LAI may be compensated by the foliar clumping which tends to give an underestimation of the PAI by DHP. [12].

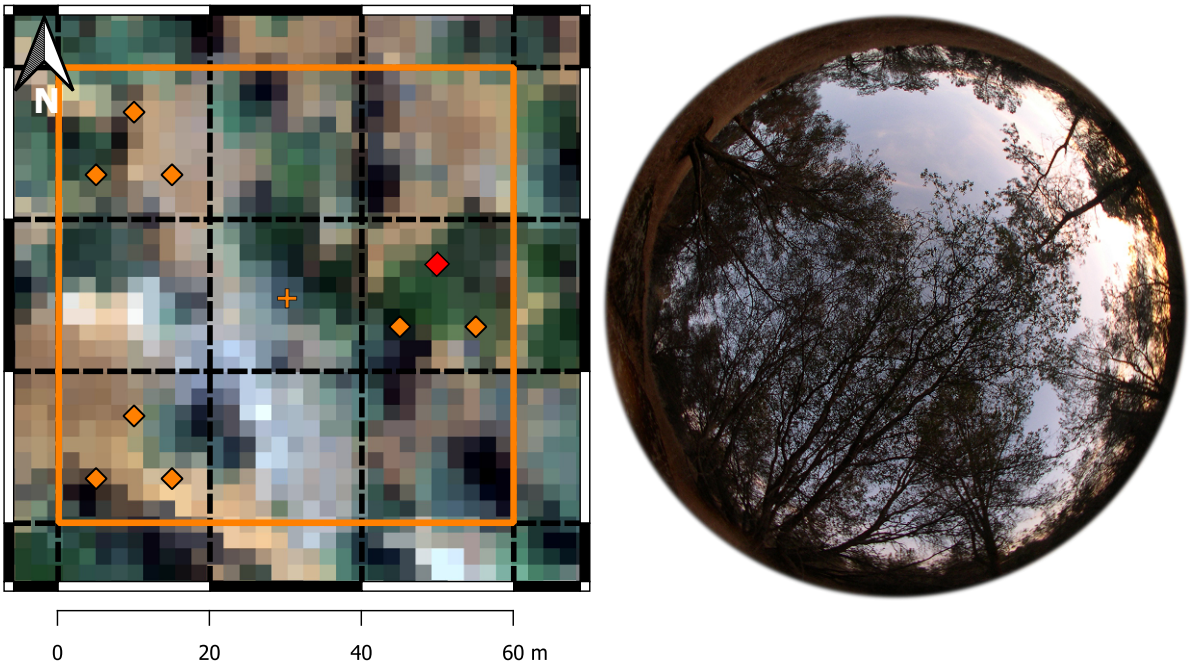


**(a)** Plot 7 location overlaid on AV-NG 2.1 m image **(b)** Example of a hemispherical photograph

**Figure 3.6:** Digital hemispherical photography acquisitions. Figure (a) shows location of the 60 m × 60 m grid of plot 7. Cross: plot center. Diamonds: DHP acquisitions, red is the one depicted in (b)

| Tree ID | 716 | 718 | 725 | 726 | 116 | 118 |
|---|---|---|---|---|---|---|
| **Species** | QUDO | QUDO | QUDO | QUDO | QUWI | QUWI |
| **Chlorophylls a+b content ($\mu g/cm^2$)** | 32.25 | 27.61 | 41.24 | 41.86 | 28.9 | 37.24 |
| **Carotenoids content ($\mu g/cm^2$)** | 8.09 | 7.9 | 10.45 | 10.74 | 7.17 | 9.43 |
| **Dry matter content ($g/cm^2$)** | 0.0114 | 0.0107 | 0.0125 | 0.0107 | 0.0158 | 0.0179 |
| **Equivalent water thickness (cm)** | 0.0101 | 0.0092 | 0.0107 | 0.0095 | 0.0119 | 0.0147 |
| **Plot ID** | | | **6** | **7** | **11** | **16** |
| **Dominant Species** | | | QUWI | QUWI | QUDO | QUDO |
| **Leaf Area Index ($m^2/m^2$)** | | | 0.75 | 0.86 | 0.23 | 0.85 |

**Table 3.1:** Biochemistry and LAI measured on site during Summer 2014

## 3.2 General Methodology

A summary of every phase of the methodology followed in this study is given in the current section. An overview of the steps listed in the following subsections is shown in 3.7.

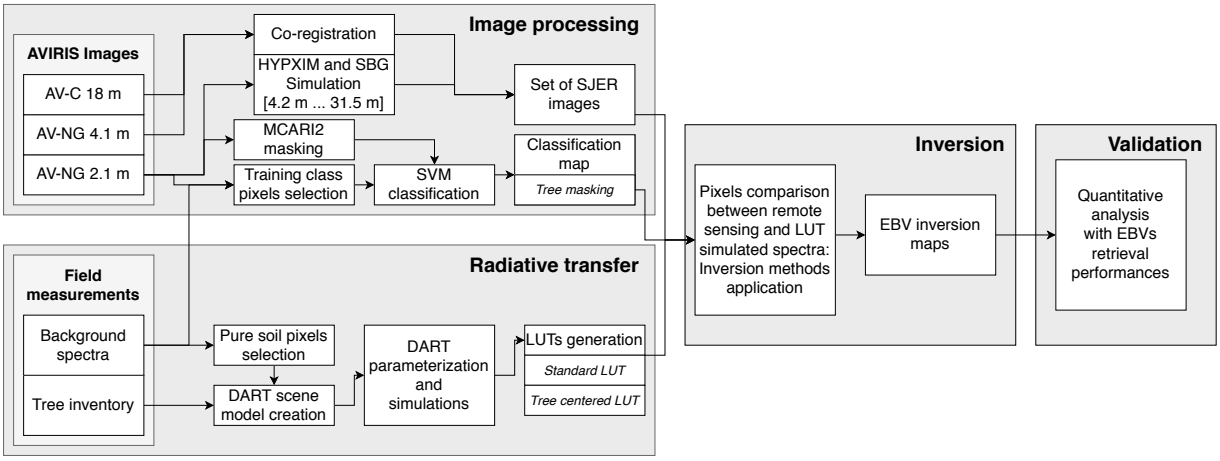


**Figure 3.7:** Methodology followed for the internship

### 3.2.1 Image processing

#### Image co-registration

The airborne images were taken on different days and with different flight paths, the AV-C and AV-NG images seemed spatially offset (non-linearly) by a few pixels. In order to improve the spatial match between the AV-C and AV-NG images a co-registration was done to obtain the same coordinate system between the images. The AV-NG image with its 2.1 m spatial resolution was chosen as reference image because its georeferencement seemed correct when overlaid with satellite maps (Bing Maps and Google Maps) in the QGIS software (https://www.qgis.org/).

A total of 25 ground control points were carefully chosen on both images (AV-NG 2.1 m and AV-C 18 m) to perform a nearest-neighbor resampling limited to rotation, scaling and translation (RST) transformations. The ground control points were chosen by finding features which were identifiable on both images. The final Root-Mean-Square Error (RMSE) of the co-registration was less than one pixel. The result of the co-registration is presented in Figure 3.8. The same approach was done for both AV-NG 2.1 m and AV-NG 4.1 m.

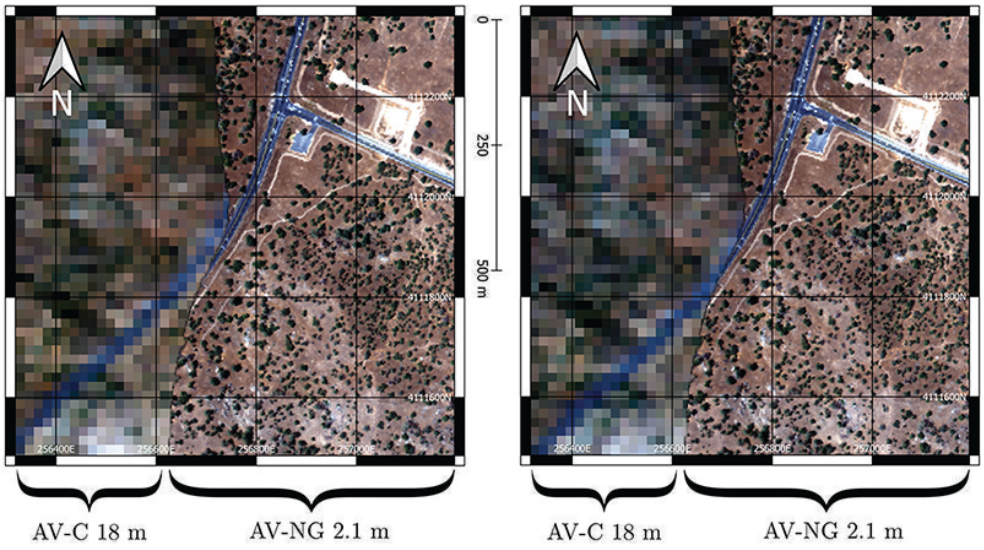


(a) Before image co-registration

(b) After image co-registration

**Figure 3.8:** Result of image co-registration between AV-C and AV-NG. The pixel offset emphasized by the road in the middle of the image (a) is reduced after the image co-registration (b).

### HYPXIM image simulations for spatial resolutions better than 30 m

One of the objectives of the internship was to assess the performance of the HYPXIM / BIODIVERSITY space mission, especially the influence of spatial resolution on the EBVs estimates.

The HYPXIM instrument targets a spatial resolution of 8 m and a spectral resolution of 0.1 µm for a spectral range from 0.4 µm to 2.5 µm. The SNR at average luminance ($L_2$) varies spectrally: 250:1 (VIS), 208:1 (Near InfraRed (NIR)), 133:1 (Short Wave Infrared (SWIR)) [13].

To simulate HYPXIM images, the AV-NG 2.1 m image was first spectrally resampled to match HYPXIM bands. Then the image was spatially resampled at different resolutions (all multiples of 2.1 up to 30 m). Finally the characteristic HYPXIM noise was added to the images. The noise was computed using tools developed at the ONERA [14], according to the HYPXIM noise model provided by the CNES with a standard deviation adjusted by the square root of the ratio between the targeted resolution and the HYPXIM resolution of HYPXIM (8 m). The image generated at 31.5 m was used as the SBG image reference because the SBG noise characteristics were unavailable. Simulated images are shown on Figure 3.9.

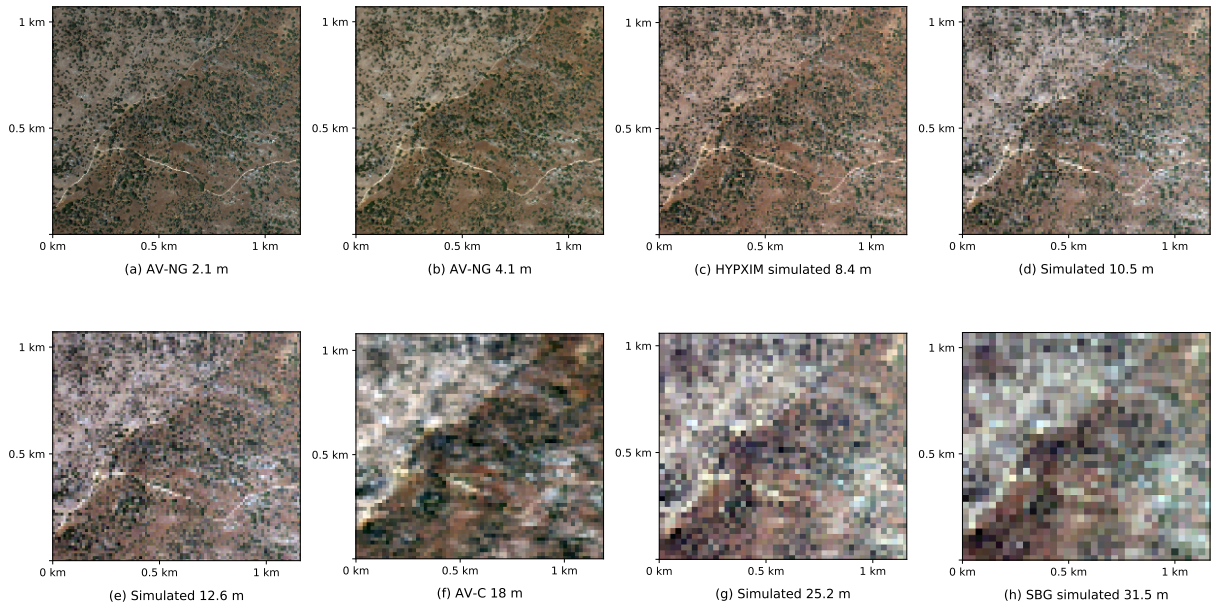


**Figure 3.9:** Simulations images up to 30m

### Vegetation masking

In order to be able to estimate broad-leaved trees' foliar pigments, it was necessary to be able to locate them on each image. An essential first step was to mask the vegetation in the images. This first masking was done using the hyperspectral Vegetation Index (VI) Modified Chlorophyll Absorption Ratio Index (MCARI) [15], a value between 0 and 1 that responds to chlorophyll variation (version 2 includes a soil adjustment factor). The VI was chosen because this can easily differentiate the tree canopy from the grass which is dry or dead (no chlorophyll) during summer.

The value of MCARI2 was calculated for each pixel of the AV-NG 2.1 m image then a threshold was used to generate the mask, the MCARI2 threshold value being chosen with the help of the histogram of the values. The results of this thresholding is shown on Figure 3.10. This mask was then processed to get a Canopy Cover (CC) map for other spatial resolutions: the mask was spatially resampled with pixel aggregation. The CC value represents the fraction of vegetation in a given pixel, the CC maps will be used later to filter pixels containing a specific percentage of vegetation.

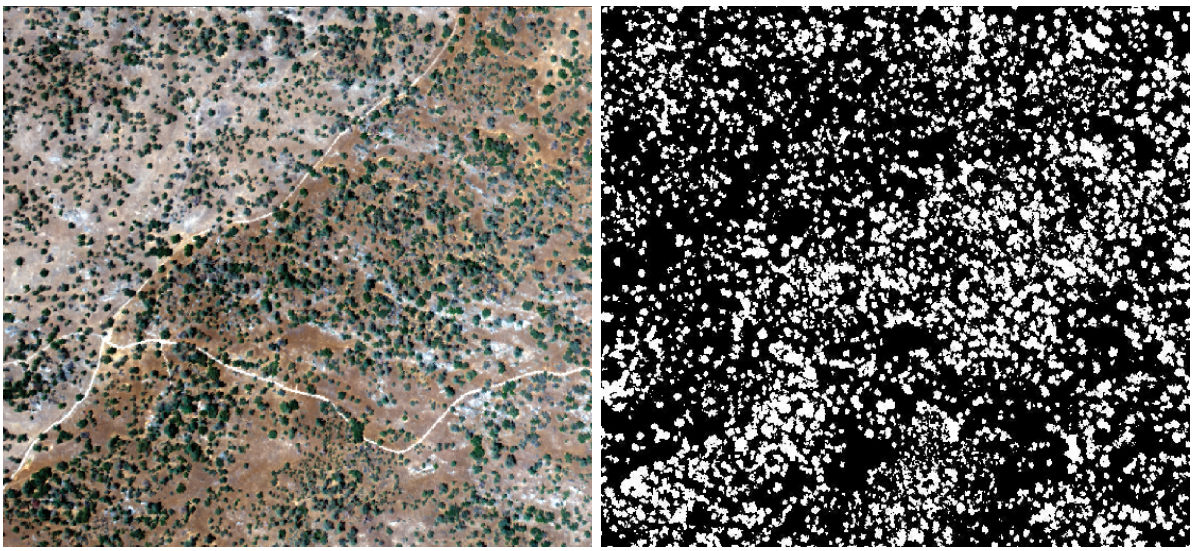

**(a)** RGB image **(b)** MCARI2 mask (white is vegetation)

**Figure 3.10:** MCARI2 masking of the AV-NG 2.1 m image

### 3.2.2 Classification map using supervised vector machine

To have a better understanding of the studied area, it was decided not only to have a mask for the broad-leaved trees but several classes for different tree species and also for different type of soil. Classification was done using Support Vector Machine (SVM) supervised learning methods [16]. Different classes were manually chosen beforehand using QGIS. A total of nine distinct pixel classes were selected: QUDO, QUWI, PISA, dirt path, rocks, litter, senescent grass, shadow and mixed soil types (as we were not able to distinguish other specific soil type). Between 410 and 450 pixels were selected for each class on the AVNG 2.1 m image to form the training dataset for the classifier (Figure 3.11 shows the average spectra of each selected class). It is important to have at least the same number of training spectra as there are bands in the image to make the classification, otherwise the classifier cannot correctly adjust all of its parameters (which correspond to the bands). The pixels were selected according to their visual aspect (using images at 1 m spatial resolution taken at different times of the year) and with the help of field measurements of spectra of different types of soil and rocks.

A random grid search found the best parameters for the classifier. The SVM classifier had the radial basis function as kernel function with a $\gamma$ coefficient of 0.0055 and a soft margin parameter $C = 6.5$.

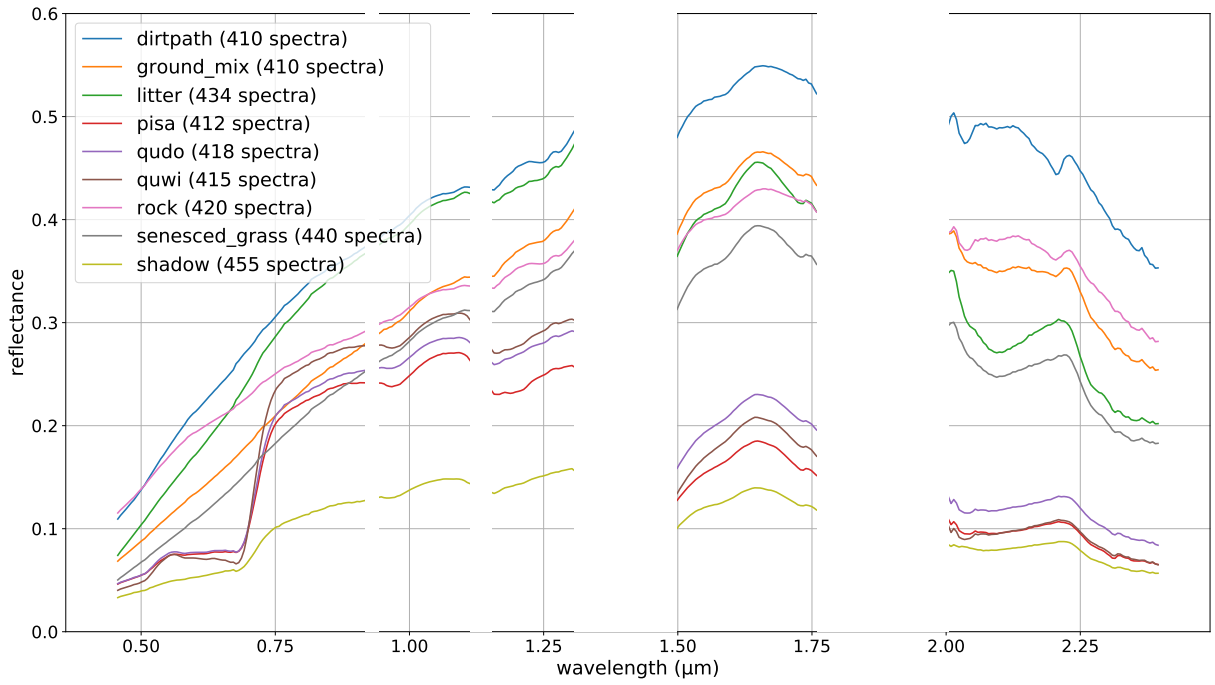


**Figure 3.11:** Spectra of the training dataset of the SVM classifier

### 3.2.3 DART software

Developed since 1993, DART (available at https://dart.omp.eu) is one of the most comprehensive three-dimensional (3D) RT models. Many Universities, research centers and space agencies use it (CNES, NASA, ...). It was patented in 2003. The Université Paul-Sabatier of Toulouse distributes its licenses. DART simulates radiation propagation over the entire optical domain (UltraViolet (UV), VIS, NIR,Far Infrared (FIR), Thermal InfraRed (TIR)) in 3D natural (forest, grass,...) and urban (buildings,...) landscapes, with topography and atmosphere.

Landscapes, hereafter called "scenes", are arrays of cells (voxels). Scene elements are simulated as a 3D juxtaposition of cells that contain turbid vegetation, fluids air, soot, water,...) and planar elements (triangles). "Turbid" is a statistical representation of matter: infinite number of infinitely small flat surfaces with an angular distribution ($sr^{-1}$), an area volume density ($m^2/m^3$), and optical properties (lambertian and/or specular).

Fluids are defined by their particle density, cross section, single scattering albedo and scattering phase function. Any triangle has a given orientation, area and optical property (Lambertian / Hapke / specular reflectance and isotropic / direct transmittance). They are used to model house, vegetation,... DART simulates directly simple landscapes and can import complex 3D scenes and scene elements with multispectral SQL databases that specify the geometric and optical properties of the atmosphere and the optical properties of landscape elements (vegetation, building,...). Different simulation methods are possible depending on the scenes and observation mode to simulate. Its iterative flux tracking mode [6] uses a finite number of discrete directions to simulate the RB and images of optical airborne and satellite radiometers). Its "LiDAR" mode ("RayCarlo" method that combines Monte Carlo and flux tracking methods simulates terrestrial airborne and satellite Lidar signal (waveform, cloud point and photon counting). Its "Lux" mode uses an efficient Monte Carlo method for fast simulations of RS images of large landscapes.

#### Creation of the scene in DART

The scene modeling in DART for the SJER site is derived from the scene modeled in a previous study on the Tonzi Ranch (TONZI) site [2]. It is based on a simplified representation of a forest.

The scene in DART represents a square area of the forest repeated an infinite number of times on a grid. The pattern is composed of four trees with ellipsoidal crowns. The scene dimensions were calculated using the projected area of the trees crown in order to simulate different canopy covers for the scene. Trees are placed in such a way that the scene Bidirectional Reflectance Factor (BRF) is the closest to a forest BRF [17, 18]. The scene is depicted in Figure 3.12.

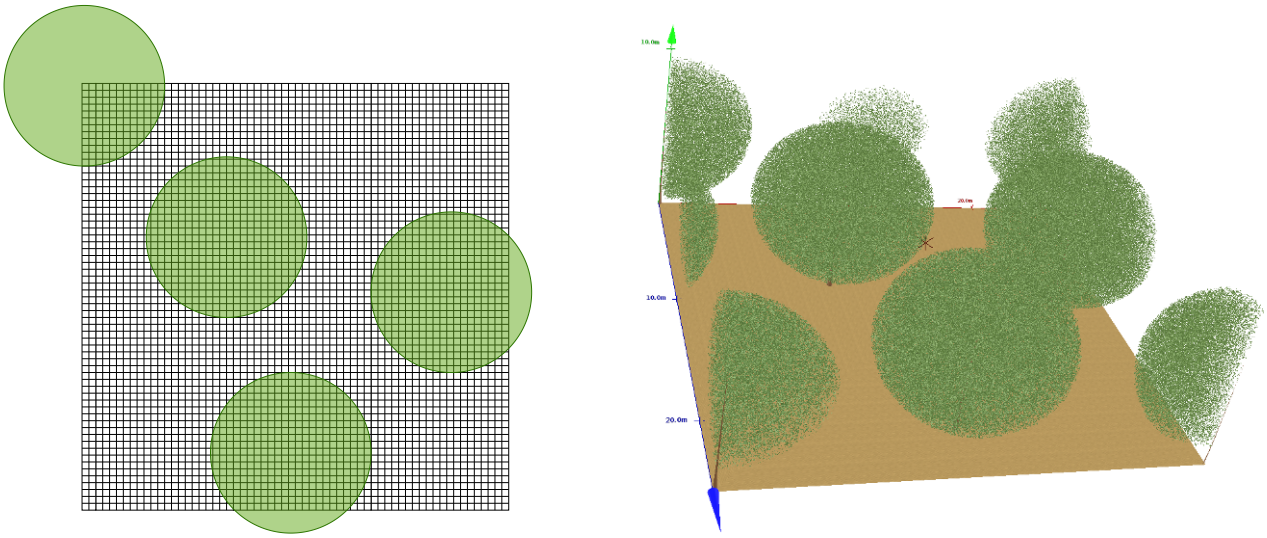

**(a)** Scene grid representation **(b)** Scene 3D view

**Figure 3.12:** SJER scene for CC 50 % in DART

The trees characteristics (crown height, crown width, ...) were set according the average QUDO values of the SJER site tree inventories over the last years (overview at Table 3.2 and trees input for DART at Table 3.3). Twigs and branches of the crown were not considered for this work as it introduces too much modeling complexity and even errors if done incorrectly.

| Tree characteristics | Median | Average | Standard deviation |
|---|---|---|---|
| Diameter at Breast Height (m) | 0.314 | 0.338 | 0.158 |
| Crown Width 1 (m) | 10.95 | 10.262 | 3.64 |
| Crown Width 2 (m) | 9 | 8.631 | 3.495 |
| Crown Height (CH) (m) | 8.4 | 9.831 | 5.209 |
| Trunk Height (TH) (m) | 9.6 | 9.312 | 2.494 |
| Ratio $\frac{\text{CH}}{\text{TH}}$ | 0.826 | 0.814 | 0.01 |

**Table 3.2:** QUDO tree inventory campaigns overview (5 campaigns between 2013 and 2015)

Trunk reflectance was set to the average value of several spectra measured in-field, although as we will see later, this does not have a significant influence. The soil under the trees (forest understory) was represented as a lambertian surface with optical properties determined by carefully chosen soil pixels (considered as pure soil, chosen in open parts of the site) from the AV-NG image in QGIS for the simulated images (pixels from the AV-C image were selected for the 18 m resolution image). Tree leaves optical properties

| Parameters | Values |
|---|---|
| **General settings** | |
| Scene dimensions $x \times y$ ($m^2$) for: | |
| CC 10 % | $55.6 \times 55.6$ |
| CC 30 % | $32.0 \times 32.0$ |
| CC 50 % | $24.8 \times 24.8$ |
| CC 70 % | $20.8 \times 20.8$ |
| CC 90 % | $18.4 \times 18.4$ |
| Voxel size $x \times y \times z$ ($m^3$) | $0.4 \times 0.4 \times 0.4$ |
| **Tree characteristics** | |
| Tree height (m) | 9.6 |
| Crown shape | ellipsoidal |
| Crown diameter (m) | 9.97 |
| Crown height (m) | 8.4 |
| Trunk height (below & within crown) (m) | $1.2, 5.6$ |
| Trunk diameter at breast height (m) | 0.31 |

**Table 3.3:** DART inputs for the scene modeling

are generated with the leaf RTM PROSPECT, which is implemented in DART [19] using a range values of inputs (detailed in Table 3.4) to generate all of the different LUT cases. The only radiation sources considered were the Sun and the atmosphere. The Sun was set to its position on the date and time of the AV-NG and AV-C image acquisitions. The atmosphere model was a DART implemented one corresponding to mid-latitude summer standard atmosphere.

### Simulations and LUT generation

The simulations were made using DART version 5.7.6 build:*1157* using the "Lux" mode as it is faster than its standard flux tracking mode and results are very similar. A total of 49280 simulations has been ran for a total of approximately 1200 CPU hours of runtime on a computing server. The parameters for each simulations are detailed in Table 3.4. Both VIS and SWIR domains were covered by the simulations with 107 bands of 0.010 µm spectral bandwith between 0.35 µm and 2.42 µm (atmospheric water absorption bands were not considered beforehand to gain time on simulation).

Each simulation generates an 1 m resolution image with 107 spectral bands. An example image is given in Figure 3.13a.

It has been considered to generate 2 LUTs, one at a tree scale using only pixels of tree (no soil) and another standard one at a population scale with pixels of tree and soil.

| Variable | Range | Step size | # of values |
|---|---|---|---|
| Chlorophylls a+b content ($C_{ab}$) (µg/cm$^2$) | 10-60 | 5 | 11 |
| Carotenoids content ($C_{car}$) (µg/cm$^2$) | 2-16 | 2 | 8 |
| Dry matter content ($C_m$) (g/cm$^2$) | 0.007-0.016 | 0.003 | 4 |
| Equivalent water thickness ($C_w$) (cm) | 0.007-0.016 | 0.003 | 4 |
| Leaf Area Index (LAI) (m$^2$/m$^2$) | 0.1-1.9 | 0.3 | 7 |

**Table 3.4:** DART vegetation input parameters for the LUT

To generate the standard simulated spectral database called LUT, at the end of each simulation the average reflectance of the images are added to the LUT for each band. These average reflectances are associated in the LUT with the simulation parameters. The LUT is composed of one table: *sjer_seq_mean(id, CC, LAI, $C_{ab}$, $C_{car}$,$C_m$, $C_w$ , $\rho_{0.35}$, ..., $\rho_{2.42}$)* with a total of 49280 rows representing the reflectance of all different scenarios simulated by DART. The second LUT was generated using only the tree centered pixels of the simulation image as the pixels to estimate contain little to no soil information at this spatial resolution. Figures 3.13b and 3.14 represents how the pixels were selected and their respective entry in the LUTs. In order to have a full performance comparison between the LUTs, both have been tested on all spatial resolutions available.

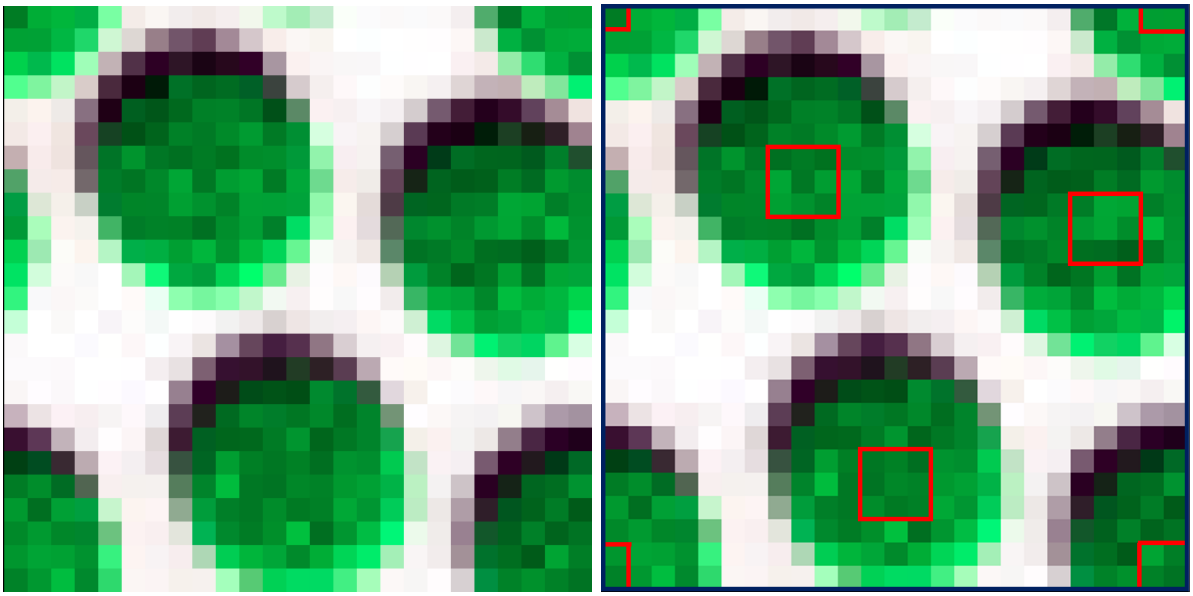

**(a)** **(b)**

**Figure 3.13:** (a): Resulting image of one DART simulation (R: 664 nm, G: 548 nm, B: 472 nm). (b): LUT pixels selection on each simulation. Blue contour is the pixels selection for the standard LUT and the red ones are for a tree centered pixels LUT.

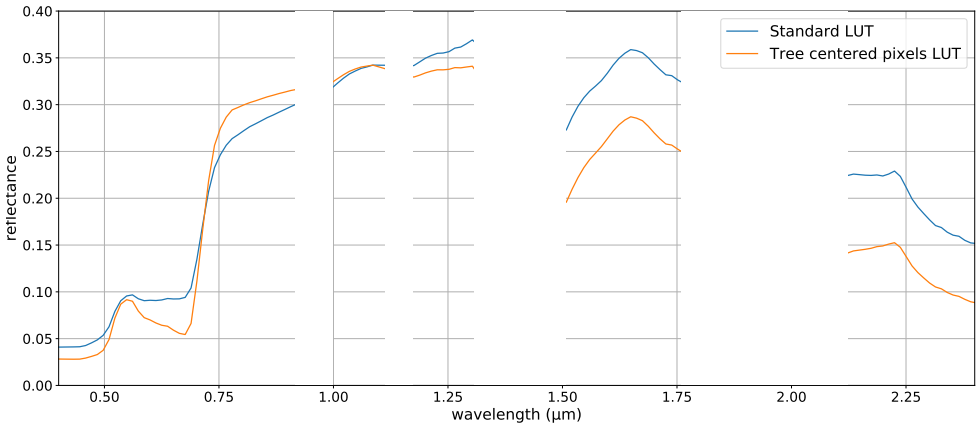


**Figure 3.14:** Reflectance spectra for both LUTs.Both spectra registered in the LUTs entry for $CC = 50\%$, LAI $= 1.9$, $C_{ab} = 30$ µg/cm$^2$, $C_{car} = 14$ µg/cm$^2$, $C_w = 0.016$ g/cm$^2$, $C_m = 0.013$ cm.

### 3.2.4 LUT-based inversion strategies

From the LUT generated with the DART simulated images, the goal was to estimate the biochemical properties of the vegetation pixels by minimizing a cost function comparing the measured reflectances of the pixels and the reflectances simulated by DART. Different cost functions were used because they have already shown promising results on the TONZI site [2]: RMSE (Equation 3.1), Spectral Angle Mapper (SAM) (Equation 3.2, it determines the spectral similarity between two spectra by calculating a spectral angle which is defined as the angle between the two spectra treating them as vectors in a space with dimensionality equal to the number of bands) and the difference between the considered VI (Equation 3.3). The LUT biophysical-chemical parameters associated to the minimizing spectra are considered to be the estimates. It is likely that several sets of parameters lead to similar reflectances for a pixel, so the average of the $q$ best minimizing parameters was considered to be the final estimation.

$$RMSE(y, \hat{y}) = \sqrt{\frac{1}{N}\sum_{i=1}^{N}(y_i - \hat{y}_i)^2} \tag{3.1}$$

$$SAM(y, \hat{y}) = \arccos\left(\frac{\sum_{i=1}^{N} y_i \hat{y}_i}{\sqrt{\sum_{i=1}^{N} y_i^2}\sqrt{\sum_{i=1}^{N} \hat{y}_i{}^2}}\right) \tag{3.2}$$

$$D_{VI}(y, \hat{y}) = abs\left(VI(y) - VI(\hat{y})\right) \tag{3.3}$$

The number $q$ of best solutions was set to 0.5% of the number of cases in the LUT for all variables to be estimated, trying to optimize this parameter could have been time-consuming for the internship and this number gave acceptable results in a previous study and was shown to be sufficient in the literature [20].

The RMSE and SAM were calculated for spectral intervals specific to the estimated variable because they each have varying impacts at certain wavelengths (see Figure 2.1). Part of the VIS spectrum was considered for $C_{ab}$ (0.5 µm - 0.75 µm) and $C_{car}$ (0.5 µm - 0.55 µm) whereas bands between 0.8 µm and 1.3 µm were used for $C_m$ and SWIR for $C_w$ (1.3 µm - 2.5 µm). The NIR and SWIR were chosen for LAI (0.8 µm - 2.5 µm). For the selection of VI to use in $D_{VI}$, several indices used in previous studies were considered. In order to identify the indices presenting the strongest variations that would justify a possible inversion with the LUT (bijective function), a look at the variation of each of these indices on the LUT cases was done (some examples are shown in Figure 3.15). Indeed, reflectances of pixels with a low CC don't necessarily show a noticeable red-edge increase nor a chlorophylls reflectance peak at 0.55 µm. As the Figure 3.15c shows and concurs with Miraglio's work [2], indices for LAI predictions are saturating at 0.4 $m^2/m^2$ LAI and above for the 10% CC cases. These cases were therefore discarded when doing the estimations. All the selected VIs formulas are detailed in Table 3.5.

To evaluate the results with field measurements, several validation metrics were considered but the RMSE between the estimated and measured values was the main indicator within the framework of the internship. Indeed, another efficient validation metric is the coefficient $R^2$ of the linear regression of the estimated vs measured scatter plot, but not enough validation points were available to have relevant $R^2$ estimations as the present study focuses only on one date.

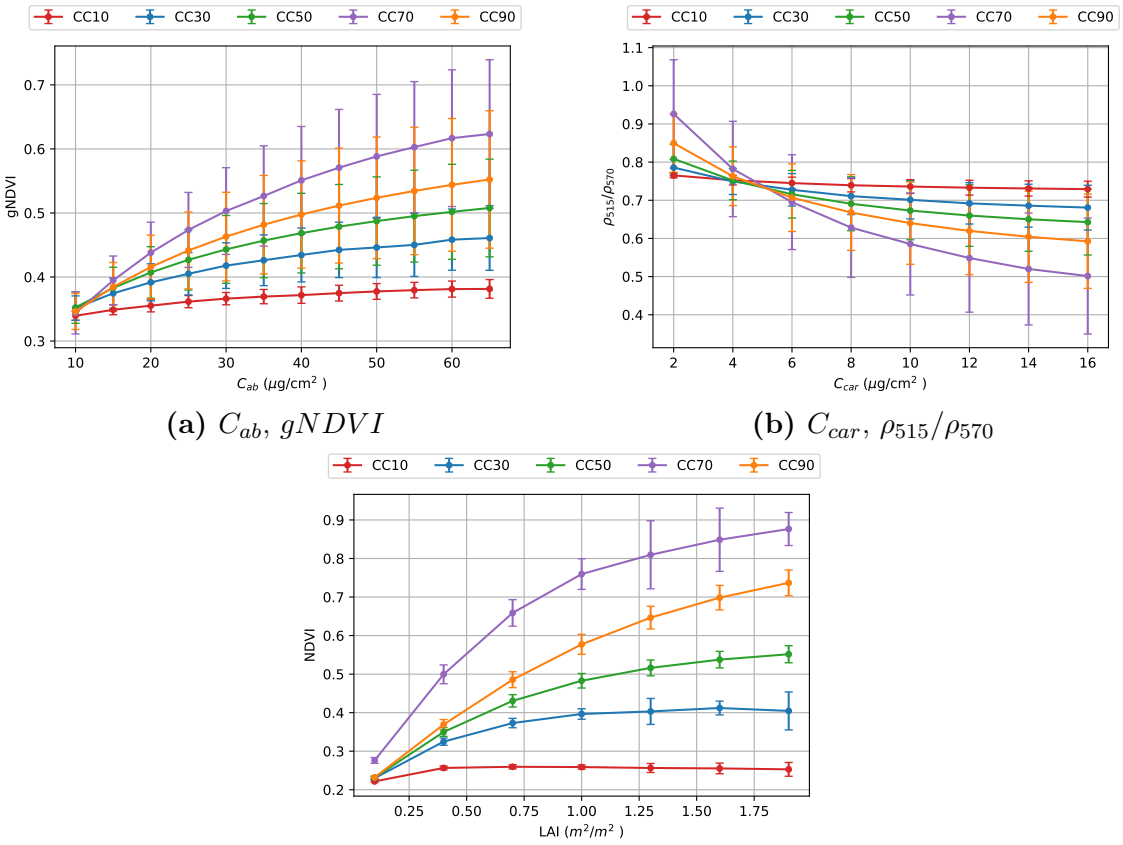


**(a)** $C_{ab}$, $gNDVI$ **(b)** $C_{car}$, $\rho_{515}/\rho_{570}$

**(c)** LAI, $NDVI$

**Figure 3.15:** VIs variation within the LUT cases. Each line represents the average VI of all the considered CC cases in the LUT. The vertical bars represent the standard deviation of these same cases.

| Variable | Method | # of bands | VI formula (wavelength in μm) | Reference |
|---|---|---|---|---|
| $C_{ab}$ | RMSE INT CAB | 19 | | |
| | SAM INT CAB | 19 | | |
| | $D_{Maccioni}$ | 3 | $\frac{\rho_{0.780}-\rho_{0.710}}{\rho_{0.780}-\rho_{0.680}}$ | [21] |
| | $D_{gNDVI}$ | 2 | $\frac{\rho_{0.780}-\rho_{0.550}}{\rho_{0.780}+\rho_{0.550}}$ | [22] |
| | $D_{GM_94b}$ | 2 | $\frac{\rho_{0.750}}{\rho_{0.550}}$ | [23] |
| | $D_{MCARI2}$ | 3 | $1.5\frac{2.5\left(\rho_{0.800}-\rho_{0.670}\right)-1.3\left(\rho_{0.800}-\rho_{0.550}\right)}{\sqrt{\left(2\rho_{0.800}+1\right)^2-\left(6\rho_{0.800}-5\sqrt{\rho_{0.670}}\right)-0.5}}$ | [15] |
| | $D_{TCARI/OSAVI}$ | 4 | $3\frac{\left(\rho_{0.700}-\rho_{0.670}\right)-0.2\left(\rho_{0.700}-\rho_{0.550}\right)\frac{\rho_{0.700}}{\rho_{0.670}}}{1.16\frac{\rho_{0.800}-\rho_{0.670}}{\rho_{0.800}+\rho_{0.670}+0.16}}$ | [24] |
| $C_{car}$ | RMSE INT CAR | 4 | | |
| | SAM INT CAR | 4 | | |
| | $D_{\rho_{515}/\rho_{570}}$ | 2 | $\frac{\rho_{515}}{\rho_{570}}$ | [25] |
| | $D_{CRI}$ | 2 | $\frac{1}{\rho_{515}}-\frac{1}{\rho_{550}}$ | [26] |
| | $D_{gNDVI}$ | 2 | $\frac{\rho_{0.780}-\rho_{0.550}}{\rho_{0.780}+\rho_{0.550}}$ | [22] |
| | $D_{GM_94b}$ | 2 | $\frac{\rho_{0.750}}{\rho_{0.550}}$ | [23] |
| LAI | RMSE INT LAI | 120 | | |
| | SAM INT LAI | 120 | | |
| | $D_{NDVI}$ | 2 | $\frac{\rho_{0.833}-\rho_{0.677}}{\rho_{0.833}+\rho_{0.677}}$ | [27] |
| | $D_{MSAVI2}$ | 2 | $\frac{1}{2}(2\rho_{0.800}+1-\sqrt{(2\rho_{0.800}+1)^2-8(\rho_{0.800}-\rho_{0.670})})$ | [28] |
| $C_w$ | RMSE INT EWT | 45 | | |
| | SAM INT EWT | 45 | | |
| | $D_{SRWI}$ | 2 | $\frac{\rho_{0.859}}{\rho_{1.240}}$ | [29] |
| | $D_{MSI7}$ | 2 | $\frac{\rho_{2.130}}{\rho_{0.859}}$ | [30] |
| $C_m$ | RMSE INT LMA | 27 | | |
| | SAM INT LMA | 27 | | |
| | $D_{NDNI}$ | 2 | $\frac{\log\frac{1}{\rho_{1.510}}-\log\frac{1}{\rho_{1.680}}}{\log\frac{1}{\rho_{1.510}}+\log\frac{1}{\rho_{1.680}}}$ | [31] |
| | $D_{NDLI}$ | 2 | $\frac{\log\frac{1}{\rho_{1.754}}-\log\frac{1}{\rho_{1.680}}}{\log\frac{1}{\rho_{1.754}}+\log\frac{1}{\rho_{1.680}}}$ | [31] |

**Table 3.5:** Spectral strategies applied for the inverse problem

# Chapter 4

# Results

## 4.1 Classification map

The final classification map of the study site is shown in Figure 4.2, we decided to categorize as "unable to class" the pixels where the classifier couldn't be at least 75% sure of the classification in order to have a classification where the pixels contain most of the class with which they were classified. The SVM classifier had a final accuracy score of 0.97 on the testing dataset (training data was split into 70%/30% for fitting/testing the classifier). As the confusion matrix shows in Figure 4.1, the distinction between QUDO and QUWI as overall their reflectance spectra are similar on some pixels (a graph of the average class spectra is depicted in Figure 3.11).

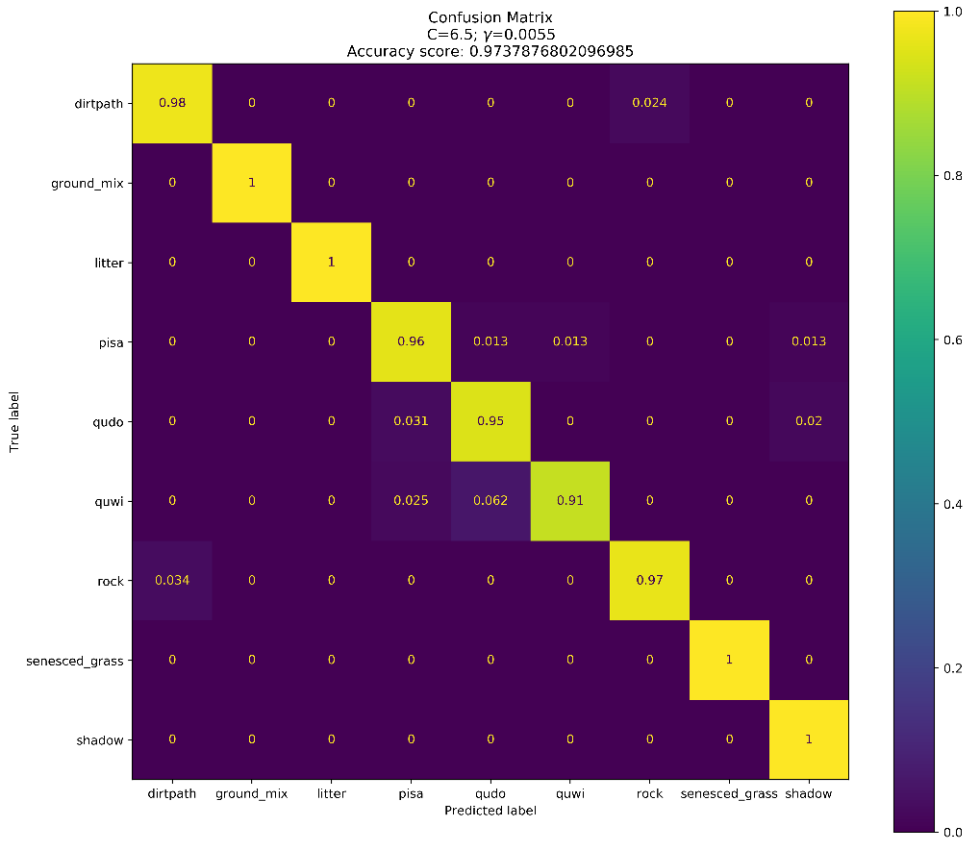


**Figure 4.1:** Confusion matrix of the SVM classifier with an accuracy score of 0.97

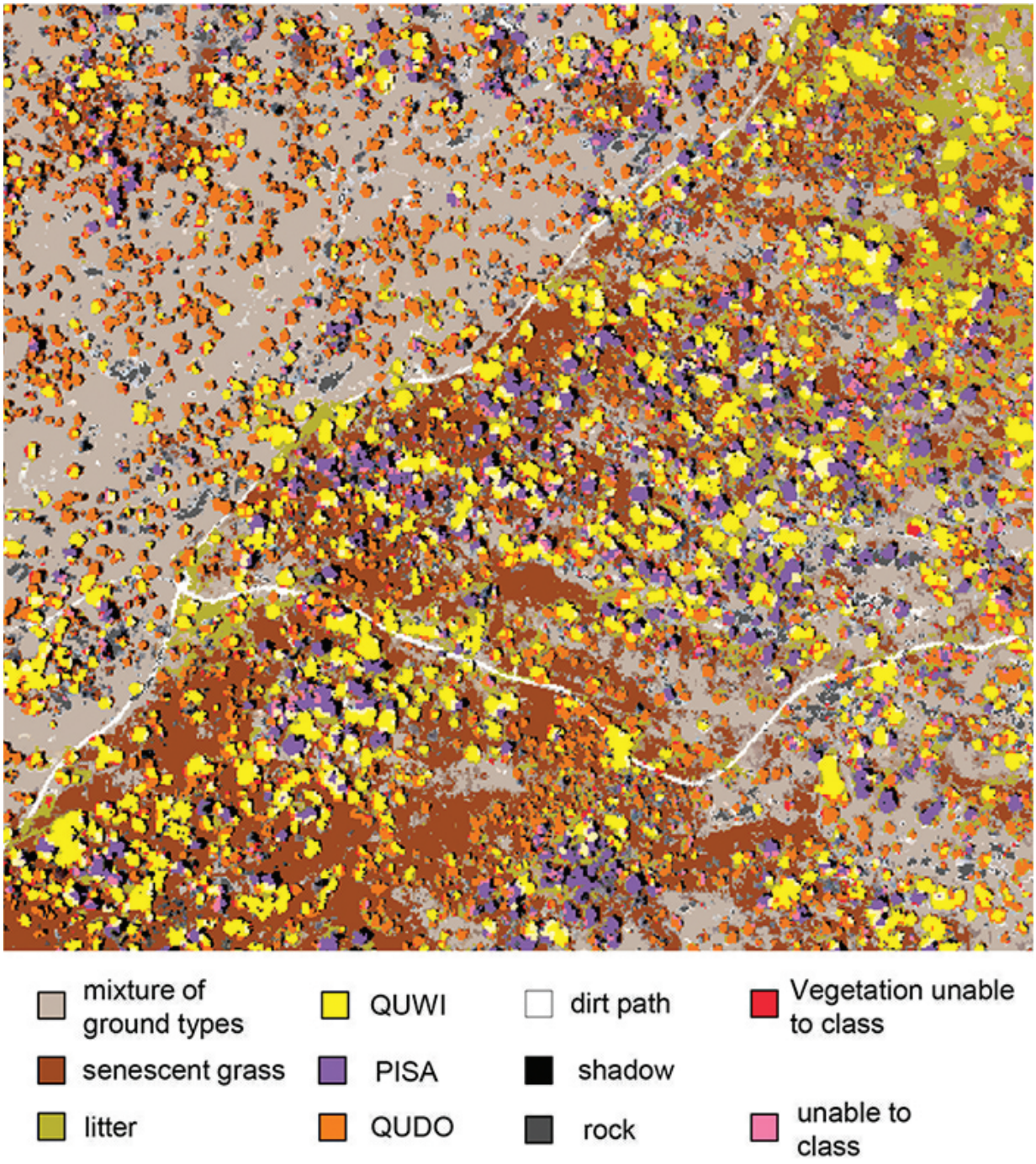


**Figure 4.2:** Classification map of the AV-NG 2.1 m image using SVM

## 4.2 LUT-based inversion

First, the reflectances generated by the DART simulations were displayed (see Figure 4.3) with the reflectances of the different AVIRIS images to check that a match could be found between the LUTs' and images' spectra, and that the modeling used in the RTM was appropriate for the SJER site.

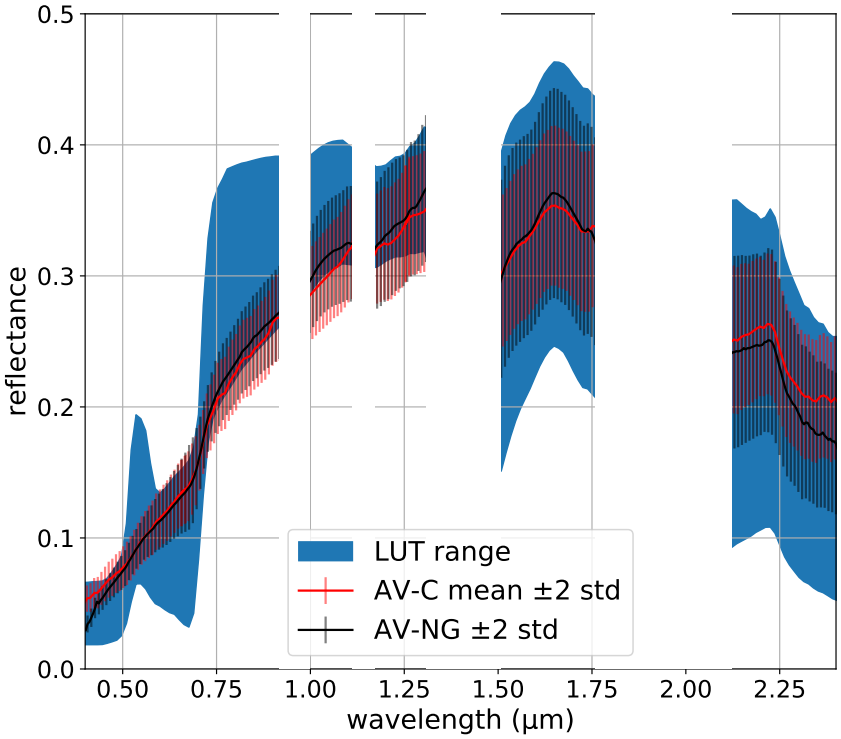


**Figure 4.3:** Reflectances computed by the DART simulations compared to reflectances of vegetation pixels within the AV-NG and AV-C image

The estimations were done on both the AV-C image at 18 m spatial resolution and the AV-NG images between 2.1 m and 31.5 m for the different LUT considered in order to assess their necessity. For the sake of readability, only HYPXIM, SBG spatial resolutions and results at different scales from all results produced are shown here, complete performances can be found found in the Appendices with Tables A.1 and A.2.

It was considered that the QUDOs and QUWIs were quite similar both in the reflectances of the pixels and physical dimensions on the SJER study site to allow us to estimate the properties of the QUWIs using the DART scene used for the estimation of those of the QUDOs. Location of ground measurements are detailed on Figure 4.4.

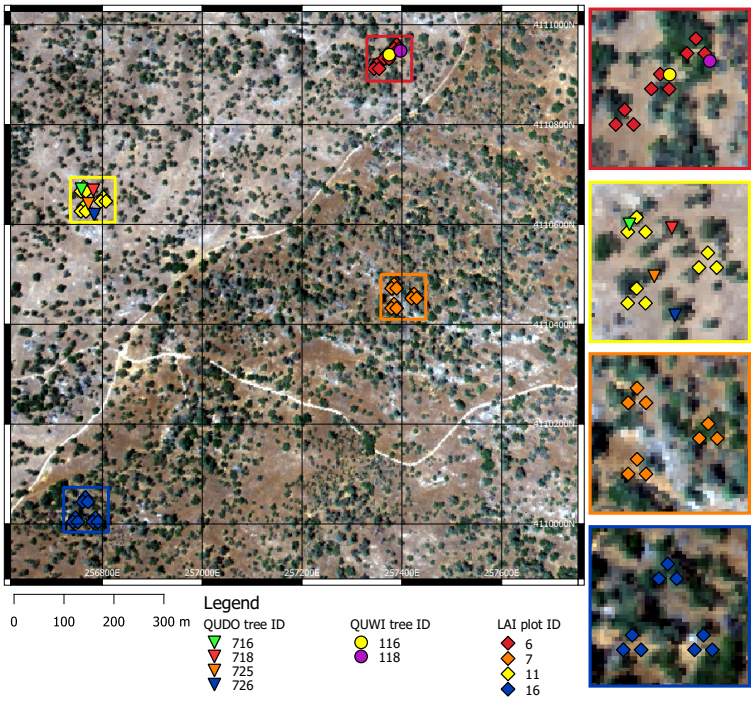


**Figure 4.4:** Biophysical-chemical measurements location for summer 2014. Triangles: QUDO trees; Disks: QUWI trees; Diamonds: DHP acquisistions

### 4.2.1 Chlorophylls a+b content ($C_{ab}$) and Carotenoids content ($C_{car}$) estimations performance

Retrieval performance data are presented in Table 4.1 for the standard LUT and in Table 4.2 for the tree centered pixels LUT. Figures 4.5 and 4.6 show examples of $C_{car}$ and $C_{ab}$ estimates for the AV-NG image at 2.1 m and 12.6 m spatial resolution with both LUTs on a measured versus estimated scatter plot.

For $C_{ab}$ estimations, all the VI differences considered, apart from $D_{TCARI/OSAVI}$, performed better than the methods based on spectral intervals (RMSE and SAM) for both LUTs and all the spatial resolutions.
With the standard LUT, $Maccioni$, $gNDVI$, and $GM_94b$ appear to be the best performing VIs RMSE wise with a mean RMSE (across all the presented spatial resolutions) of respectively 10.82 µg/cm$^2$, 10.91 µg/cm$^2$ and 11.67 µg/cm$^2$.
For the tree centered pixels with the same criteria, only $gNDVI$, and $GM_94b$ seem to be best performing VIs with a mean RMSE of respectively 8.11 µg/cm$^2$ and 8.67 µg/cm$^2$, $Maccioni$ has a mean RMSE of 11.48 µg/cm$^2$.
At 2.1 m spatial resolution, both $D_{gNDVI}$ and $D_{GM_94b}$ strategies performed better with the tree centered pixels LUT (6.45 µg/cm$^2$ and 6.38 µg/cm$^2$) than with the standard LUT (8.42 µg/cm$^2$ and 7.86 µg/cm$^2$).

| Method | Spatial resolution RMSE (µg/cm²), $R^2$ | | | | | |
|---|---|---|---|---|---|---|
| $C_{ab}$ | 2.1 m | 4.2 m | 8.4 m (HYPXIM) | 12.6 m | 18.9 m | 31.5 m (SBG) |
| RMSE INT CAB | 21.19, 0.05 | 19.20, 0.10 | 18.93, 0.01 | 21.95, 0.03 | 23.61, 0.05 | 19.67, 0.02 |
| SAM INT CAB | 5.93, 0.60 | 14.34, 0.14 | 20.23, 0.01 | 19.04, 0.20 | 20.96, 0.03 | 21.79, 0.08 |
| $D_{Maccioni}$ | 8.73, 0.25 | 7.72, 0.34 | 15.19, 0.05 | 10.91, 0.12 | 10.50, 0.08 | 11.87, 0.30 |
| $D_{gNDVI}$ | 8.42, 0.12 | 8.54, 0.07 | 13.53, 0.05 | 9.83, 0.16 | 14.97, 0.23 | 10.19, 0.25 |
| $D_{GM_94b}$ | 7.86, 0.24 | 8.65, 0.01 | 15.08, 0.03 | 12.46, 0.01 | 15.41, 0.01 | 10.69, 0.20 |
| $D_{MCARI2}$ | 6.92, 0.01 | 13.75, 0.51 | 15.36, 0.01 | 13.09, 0.42 | 14.83, 0.02 | 16.47, 0.01 |
| $D_{TCARI/OSAVI}$ | 10.10, 0.59 | 16.81, 0.01 | 18.59, 0.24 | 19.42, 0.17 | 18.96, 0.01 | 15.68, 0.55 |
| $C_{car}$ | 2.1 m | 4.2 m | 8.4 m (HYPXIM) | 12.6 m | 18.9 m | 31.5 m (SBG) |
| RMSE INT CAR | 5.32, 0.03 | 4.93, 0.13 | 5.83, 0.42 | 3.62, 0.01 | 4.39, 0.64 | 3.00, 0.29 |
| SAM INT CAR | 5.42, 0.01 | 5.39, 0.22 | 5.64, 0.42 | 4.24, 0.13 | 4.13, 0.04 | 4.73, 0.01 |
| $D_{\rho_{515}/\rho_{570}}$ | 4.49, 0.09 | 5.05, 0.40 | 3.89, 0.60 | 2.12, 0.04 | 3.84, 0.74 | 2.93, 0.18 |
| $D_{CRI}$ | 1.82, 0.25 | 3.95, 0.18 | 4.73, 0.14 | 2.53, 0.47 | 4.75, 0.67 | 4.74, 0.04 |

**Table 4.1:** RMSE of the different $C_{ab}$ and $C_{car}$ strategies estimates and the $R^2$ coefficient of the linear regression of the estimated versus measured scatter plot with the standard LUT

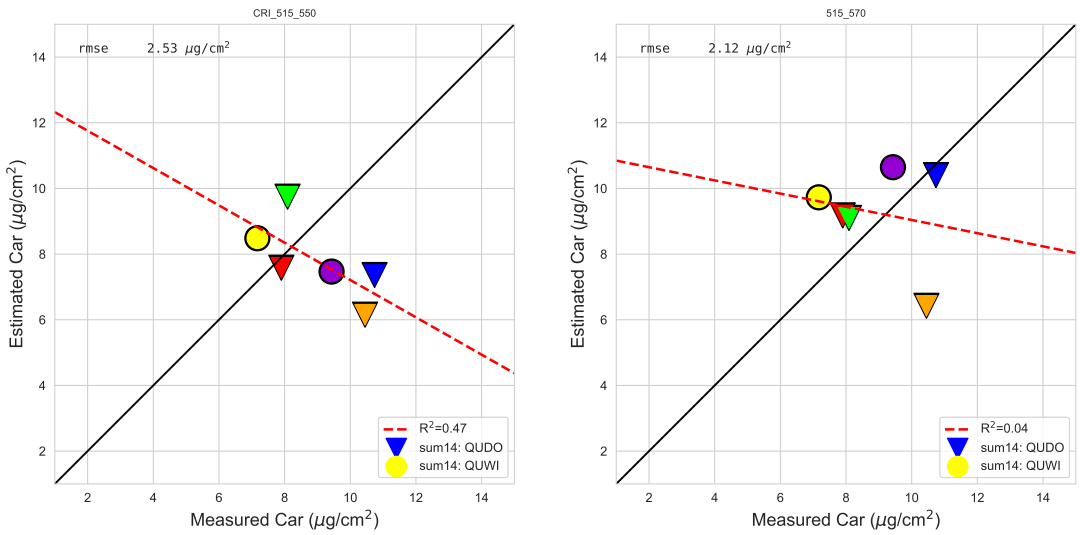


**(a)** $CRI$ **(b)** $\rho_{515}/\rho_{570}$

**Figure 4.5:** Measured versus estimated $C_{car}$ using $D_{CRI}$ (a) and $D_{\rho_{515}/\rho_{570}}$ (b) methods at 12.6 m resolution with the standard LUT

| Method | Spatial resolution RMSE (µg/cm²), R² | | | | | |
|---|---|---|---|---|---|---|
| $C_{ab}$ | 2.1 m | 4.2 m | 8.4 m (HYPXIM) | 12.6 m | 18.9 m | 31.5 m (SBG) |
| RMSE INT CAB | 20.24, 0.07 | 17.94, 0.06 | 14.67, 0.14 | 24.12, 0.36 | 21.21, 0.06 | 23.71, 0.01 |
| SAM INT CAB | 15.94, 0.40 | 21.07, 0.61 | 19.59, 0.14 | 21.90, 0.01 | 22.64, 0.01 | 22.75, 0.55 |
| $D_{Maccioni}$ | 9.92, 0.16 | 6.29, 0.49 | 14.43, 0.02 | 11.94, 0.19 | 12.32, 0.13 | 13.98, 0.13 |
| $D_{gNDVI}$ | 6.0, 0.29 | 7.08, 0.16 | 8.24, 0.24 | 10.62, 0.03 | 7.1, 0.14 | 9.15, 0.01 |
| $D_{GM_94b}$ | 6.02, 0.51 | 9.58, 0.02 | 7.25, 0.11 | 9.98, 0.18 | 8.79, 0.10 | 10.02, 0.05 |
| $D_{MCARI2}$ | 8.68, 0.34 | 9.81, 0.17 | 14.39, 0.32 | 13.61, 0.07 | 14.12, 0.09 | 13.02, 0.05 |
| $D_{TCARI/OSAVI}$ | 18.57, 0.59 | 22.94, 0.10 | 19.58, 0.01 | 23.09, 0.49 | 24.83, 0.42 | 24.10, 0.38 |
| $C_{car}$ | 2.1 m | 4.2 m | 8.4 m (HYPXIM) | 12.6 m | 18.9 m | 31.5 m (SBG) |
| RMSE INT CAR | 4.27, 0.01 | 3.85, 0.35 | 5.37, 0.31 | 4.14, 0.06 | 4.24, 0.24 | 3.56, 0.01 |
| SAM INT CAR | 4.71, 0.01 | 5.00, 0.29 | 5.66, 0.48 | 3.62, 0.48 | 5.20, 0.52 | 4.54, 0.01 |
| $D_{\rho_{515}/\rho_{570}}$ | 3.76, 0.08 | 3.69, 0.23 | 3.41, 0.66 | 2.23, 0.19 | 3.10, 0.73 | 2.37, 0.01 |
| $D_{CRI}$ | 3.67, 0.35 | 4.45, 0.67 | 4.89, 0.01 | 4.99, 0.55 | 5.10, 0.71 | 4.66, 0.01 |

**Table 4.2:** RMSE of the different $C_{ab}$ and $C_{car}$ strategies estimates and the $R^2$ coefficient of the linear regression of the estimated versus measured scatter plot with the tree centered pixels LUT

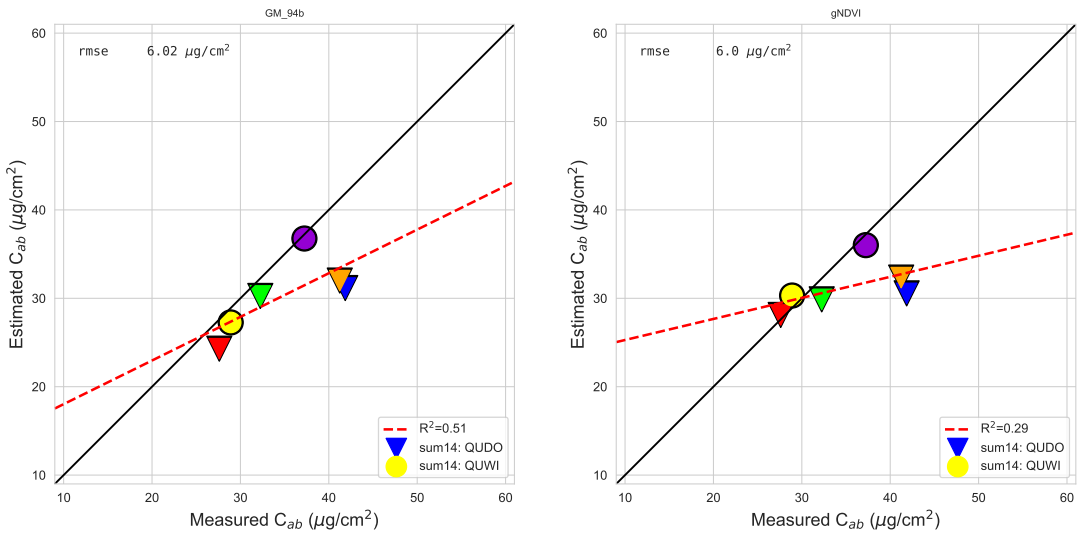


**(a)** $GM_94b$ **(b)** $gNDVI$

**Figure 4.6:** Measured versus estimated $C_{ab}$ using $D_{GM_94b}$ (a) and $D_{gNDVI}$ (b) methods at 2.1 m resolution with the tree centered pixels LUT

As expected the $R^2$ criterion performed very poorly for a lot of estimations even for the best RMSE performing ones. Figure 4.6a shows the estimates at 2.1 m spatial resolution with the tree centered pixels LUT which is one case where most $D_{GM_94b}$ estimated points are close to the first bisector ($RMSE = 6.02 \mu g/cm^2$, $R^2 = 0.51$).

For $C_{car}$ estimations, $D_{\rho_{515}/\rho_{570}}$ has overall better RMSE performance than the other strategies with an mean RMSE of 3.09 $\mu g/cm^2$ and a variable $R^2$ coefficient (from 0.01 to 0.73).

The effects of the spatial resolution on the $C_{ab}$ and $C_{car}$ estimations is not explicit, it looks like the RMSE is slightly increasing with the spatial resolution up to 31.5 m for most of the $C_{ab}$ estimation strategies and both LUTs.
Remarkably both $gNDVI$ and $GM_94b$ VIs with the tree centered pixels LUT appeared to be robust to spatial resolution as the RMSE performance stays quite low across all the spatial resolutions.

### 4.2.2 Leaf Area Index (LAI) estimations performance

Table 4.3 presents the LAI retrieval performances with the standard LUT. The best performing strategy was obtained with the method RMSE INT LAI with a mean RMSE of 0.15 $m^2/m^2$ and an overall high $R^2$ coefficient. The other three strategies SAM INT LAI, $D_{NDVI}$ and $D_{MSAVI2}$ performed similarly with an average RMSE of respectively 0.32 $m^2/m^2$, 0.28 $m^2/m^2$ and 0.33 $m^2/m^2$.
SAM INT LAI, $D_{MSAVI2}$ methods have a high $R^2$ coefficient for all spatial resolutions (above 0.9 for SAM INT LAI) while for $D_{NDVI}$ the coefficient is very low for all spatial resolutions below 18 m and the $R^2$ associated to RMSE INT LAI is decreasing when the spatial resolution increases.
The $NDVI$ VI has a steady performance across the spatial resolutions whereas the performance of the other three methods seem affected by the spatial resolution with an increasing RMSE and decreasing $R^2$ (except for $D_{MSAVI2}$).

Figure 4.7 shows examples of estimates using RMSE INT LAI and $D_{MSAVI2}$ methods at 2.1 m. The entire 31.5 m image was estimated to have a LAI map of the SJER site, the map is displayed in Figure 4.8. The study site has low LAI region in the North-West and higher LAI region in the South-East region which concurs with the AV-NG image where the tree distribution has the same pattern (Figure 3.2).

| Method | Spatial resolution RMSE ($m^2/m^2$), $R^2$ | | | | | |
|---|---|---|---|---|---|---|
| LAI | 2.1 m | 4.2 m | 8.4 m (HYPXIM) | 12.6 m | 18.9 m | 31.5 m (SBG) |
| RMSE INT LAI | 0.11, 0.93 | 0.11, 0.92 | 0.12, 0.82 | 0.15, 0.71 | 0.21, 0.49 | 0.22, 0.35 |
| SAM INT LAI | 0.26, 0.97 | 0.27, 0.96 | 0.29, 0.99 | 0.30, 0.97 | 0.28, 0.94 | 0.52, 0.90 |
| $D_{NDVI}$ | 0.30, 0.18 | 0.29, 0.09 | 0.26, 0.12 | 0.30, 0.03 | 0.26, 0.66 | 0.27, 0.94 |
| $D_{MSAVI2}$ | 0.27, 0.82 | 0.28, 0.84 | 0.30, 0.99 | 0.35, 0.76 | 0.35, 0.91 | 0.43, 0.96 |

**Table 4.3:** RMSE of the different LAI strategies estimates and the $R^2$ coefficient of the linear regression of the estimated versus measured scatter plot with the standard LUT

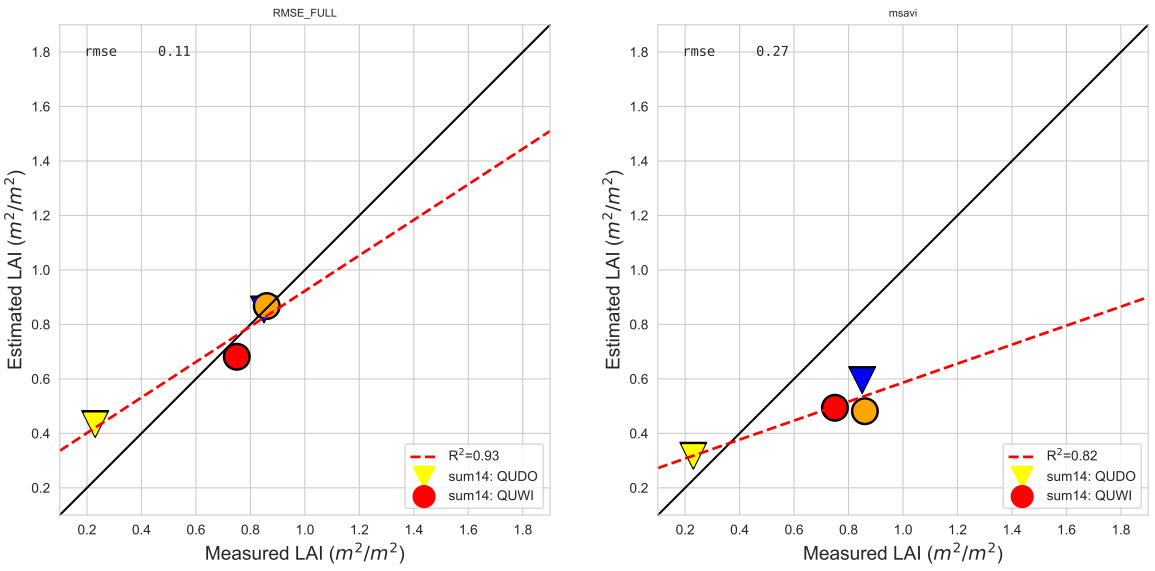


**(a)** RMSE INT LAI **(b)** $MSAVI2$

**Figure 4.7:** Measured versus estimated plot LAI using RMSE INT LAI (a) and $D_{MSAVI2}$ (b) methods at 2.1 m resolution with the standard LUT

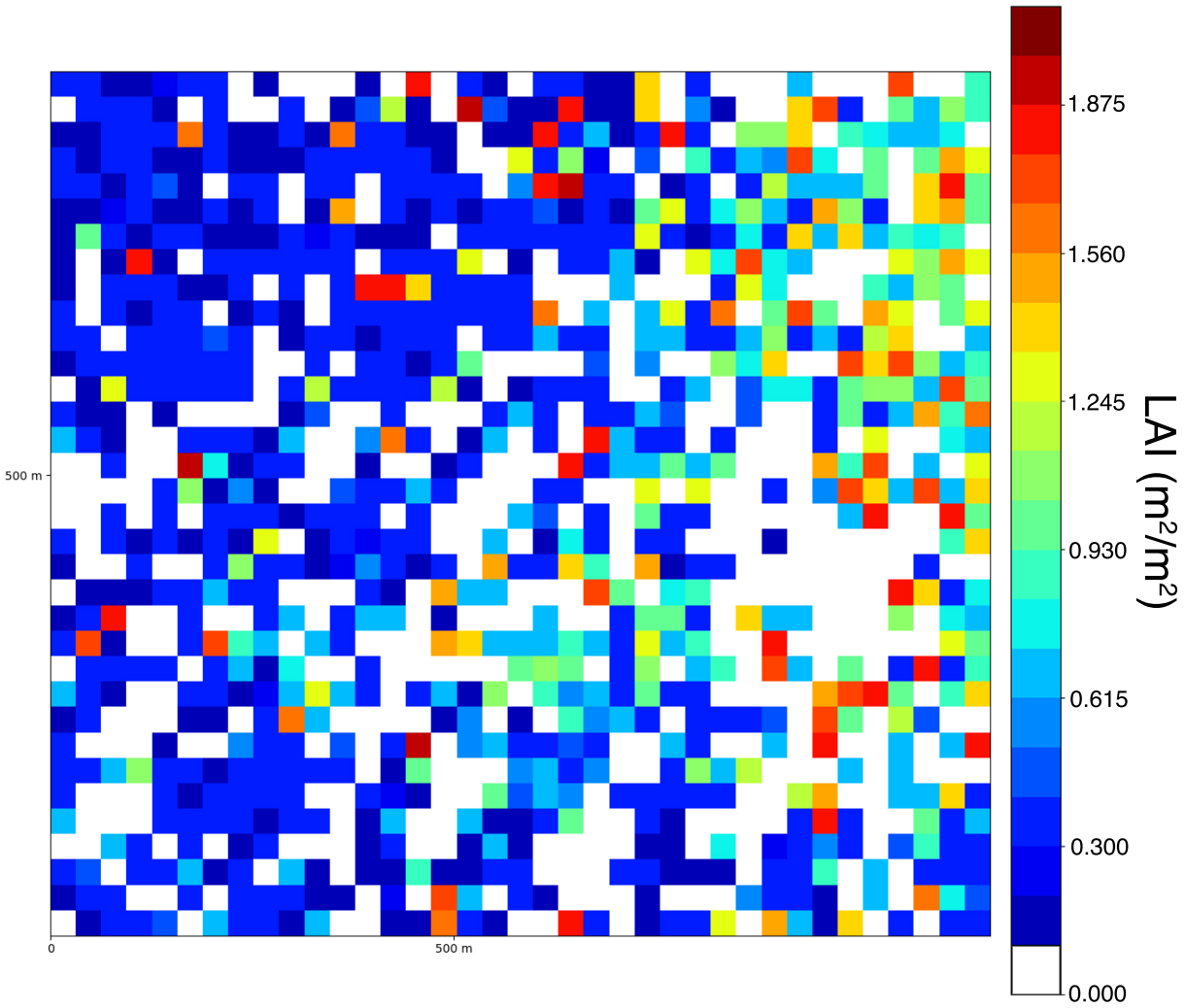


**Figure 4.8:** LAI estimation on SJER study site at 31.5 m spatial resolution using RMSE INT LAI strategy with the standard LUT. White pixels contain less than 25% vegetation information. $RMSE = 0.22$ m$^2$/m$^2$

### 4.2.3 Dry matter content ($C_m$) and Equivalent water thickness ($C_w$) estimations performance

Table 4.4 presents $C_m$ and $C_w$ retrieval performances with the standard LUT. All strategies considered showed underwhelming results for both $C_w$ and $C_m$ as the scatter plots (examples are displayed on Figure 4.9) showed no real trends as much as with the $C_{ab}$ estimations and the RMSEs were higher than other studies [32]. $D_{NDNI}$ showed best results for $C_m$ with an average RMSE of 0.0032 g/cm$^2$ and $D_{SRWI}$ with an average RMSE of 0.0027 g/cm$^2$.

| **Method** | **Spatial resolution RMSE (g/cm²), R²** | | | | | |
|---|---|---|---|---|---|---|
| $C_m$ | 2.1 m | 4.2 m | 8.4 m (HYPXIM) | 12.6 m | 18.9 m | 31.5 m (SBG) |
| RMSE INT LMA | 0.0030, 0.09 | 0.0032, 0.08 | 0.0068, 0.01 | 0.0048, 0.02 | 0.0029, 0.04 | 0.0056, 0.05 |
| SAM INT LMA | 0.0020, 0.03 | 0.0056, 0.06 | 0.0045, 0.01 | 0.0056; 0.03 | 0.0060, 0.01 | 0.0054, 0.03 |
| $D_{NDNI}$ | 0.0032, 0.01 | 0.0035, 0.03 | 0.0033, 0.05 | 0.0038, 0.04 | 0.0030, 0.07 | 0.0025, 0.40 |
| $D_{NDLI}$ | 0.0018, 0.01 | 0.0042, 0.03 | 0.0036, 0.02 | 0.0041, 0.02 | 0.0042, 0.03 | 0.0048, 0.02 |
| $C_w$ | 2.1 m | 4.2 m | 8.4 m (HYPXIM) | 12.6 m | 18.9 m | 31.5 m (SBG) |
| RMSE INT EWT | 0.0032, 0.03 | 0.0042, 0.01 | 0.0038, 0.02 | 0.0032, 0.09 | 0.0024, 0.01 | 0.0016, 0.04 |
| SAM INT EWT | 0.0031, 0.03 | 0.0035, 0.02 | 0.0036, 0.04 | 0.0036, 0.03 | 0.0025, 0.03 | 0.0023, 0.01 |
| $D_{MSI7}$ | 0.0020, 0.28 | 0.0041, 0.08 | 0.0034, 0.04 | 0.0031, 0.16 | 0.0028, 0.07 | 0.0025, 0.08 |
| $D_{SRWI}$ | 0.0018, 0.12 | 0.0027, 0.03 | 0.0026, 0.06 | 0.0027, 0.02 | 0.0034, 0.01 | 0.0032, 0.12 |

**Table 4.4:** RMSE of the different $C_m$ and $C_w$ strategies estimates and the $R^2$ coefficient of the linear regression of the estimated versus measured scatter plot with the standard LUT

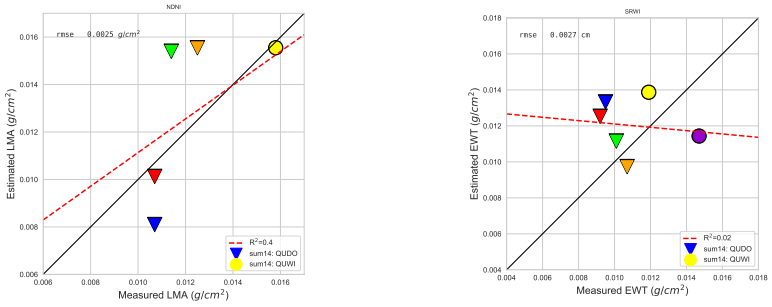


**(a)** $NDNI$, 31.5 m **(b)** $SRWI$, 4.2 m

**Figure 4.9:** Measured versus estimated leaf $C_m$ using $D_{NDNI}$ at 31.5 m (a) and $C_w$ using $D_{SRWI}$ at methods at 4.2 m resolution (b) with the standard pixels LUT

# Chapter 5

# Discussions

As stated earlier, a small number of validation points were available considering only one date in the summer of 2014 making the analysis of the results more difficult because any attempts at hypothetical explanations will have to be confirmed later by applying this same methodology on the different dates in order to have a number of validations points significant enough to be able to draw true trends from it.

## 5.1 Limitations of the results on biochemical properties

As detailed in the section 4.2.3, this methodology was applied to estimate the dry matter content and the water equivalent thickness of the leaf using different inversion strategies and VI. Although the results are encouraging for the estimation of the LAI, chlorophylls and carotenoid contents, all the strategies performed very poorly independently of the spatial resolutions with $R^2$ coefficients very close to 0 and a distribution of the estimated points which seemed random.

The VIs used for the chlorophylls content estimation such as $gNDVI$ and $GM_94b$ were also tested on the estimation of carotenoid content because they use some of the carotenoid absorption bands and presented low RMSEs (below 2 $\mu g/cm^2$ on average) as well as a very high $R^2$ coefficient regardless of the spatial resolution. It was observed soon after that these estimates behaved rather like a uniform distribution in the set of all the values available in the LUT. The facts that the average value of carotenoid content measured in the SJER study site is 8.82 $\mu g/cm^2$, that the average value of the LUT is 9 $\mu g/cm^2$, and that the estimate is an average of the $q$ best solutions explain that the estimates were so close to the truth data and the RMSEs were this low. This hypothesis was confirmed when new estimations were done from a LUT with carotenoid content parameters ranging from 6 $\mu g/cm^2$ to 16 $\mu g/cm^2$ and all estimates were centered around 11 $\mu g/cm^2$ for these VI.

## 5.2 Results distributions on the whole SJER study site

### 5.2.1 Distribution of canopy cover among the estimates

Investigations on the distribution of the values of CC chosen among the best $q$ solutions according to the VIs for the standard LUT were done (see Figure 5.1. This was done to verify if the strategies were giving coherent results and not picking only extreme CC setups even with good performances.
For the estimation of the chlorophylls contents, all the best strategies ($D_{gNDVI}$, $D_{GM_94b}$) led to equal distribution among the available CC values and all spatial resolutions (CC30%: 24.6%, CC50%: 24.8%, CC70%: 26.2%, CC90%: 24.4% in average). With the $MCARI2$ VI and the strategies based on spectral intervals, the distributions were different: $D_{MCARI2}$ tended to choose the cases with a low CC (80% of the cases chosen on average had CCs lower than 50%); the same behavior applied for SAM INT CAB but for resolutions less than 18 m (the distribution of CC values was uniform above 18 m); RMSE INT CAB seemed to favor cases of CC30% and CC90% regardless of spatial resolution (30% distribution for both on average).
Concerning the carotenoid content estimation, both $D_{\rho_{515}/\rho_{570}}$ and $D_{CRI}$ surprisingly avoided the CC70% cases of the LUT as they represented in average only 12.9% of the $q$ best solutions of the LUT for all spatial resolutions. SAM INT CAR and RMSE INT CAR strategies both chose equivalently between the values available.
Both of $NDVI$ and $MSAVI2$ had the same uniform behaviour for LAI inversion but SAM INT LAI and RMSE INT LAI favored high CC values for spatial resolutions close to 2.1 m and low CC values for the ones close to 31.5 m. This can be justified by the fact that most of the pixels selected in the plots at 2.1 m contains high percentage of vegetation and could be considered as high CC.

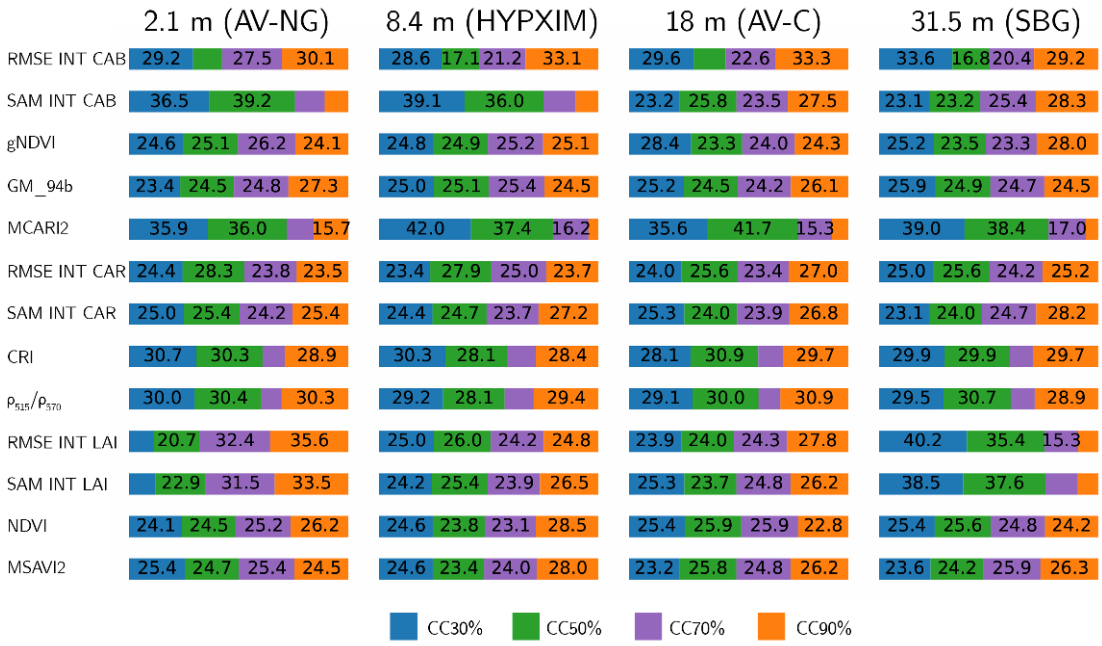


**Figure 5.1:** Canopy cover distribution among the estimates for the inversion strategies considered. Each bar represents percentage of the values of CC chosen among the best $q$ solutions according to the method for the standard LUT.

### 5.2.2 Distribution of the estimates on the whole SJER study site

Estimations were also done on all of the QUDO vegetation pixels of the images. Figures 5.2 and 5.3 show the distributions of the estimated values of $C_{ab}$ and $C_{car}$ according to the method used and the spatial resolutions; two $C_{ab}$ inversion maps at 2.1 m are displayed on Figure 5.4 using SAM INT CAB and $D_{GM_94b}$ which presented satisfying performances. Each method has its own particular distribution across spatial resolution, with a slight flattening as the resolution goes up to 31.5 m which renders a coherent behaviour of the inversion methods as the pixels are agglomerating. Both SAM INT CAB and RMSE INT CAB distributions suggest that these two methods are overestimating chlorophylls and carotenoid contents (the estimates were also overestimated for most of the spatial resolutions). Even though SAM INT CAB had the best performance at 2.1 m with a RMSE of 5.93 $\mu g/cm^2$, this concurs with the low performance of these methods for $C_{ab}$ and $C_{car}$ retrieval on the other images.

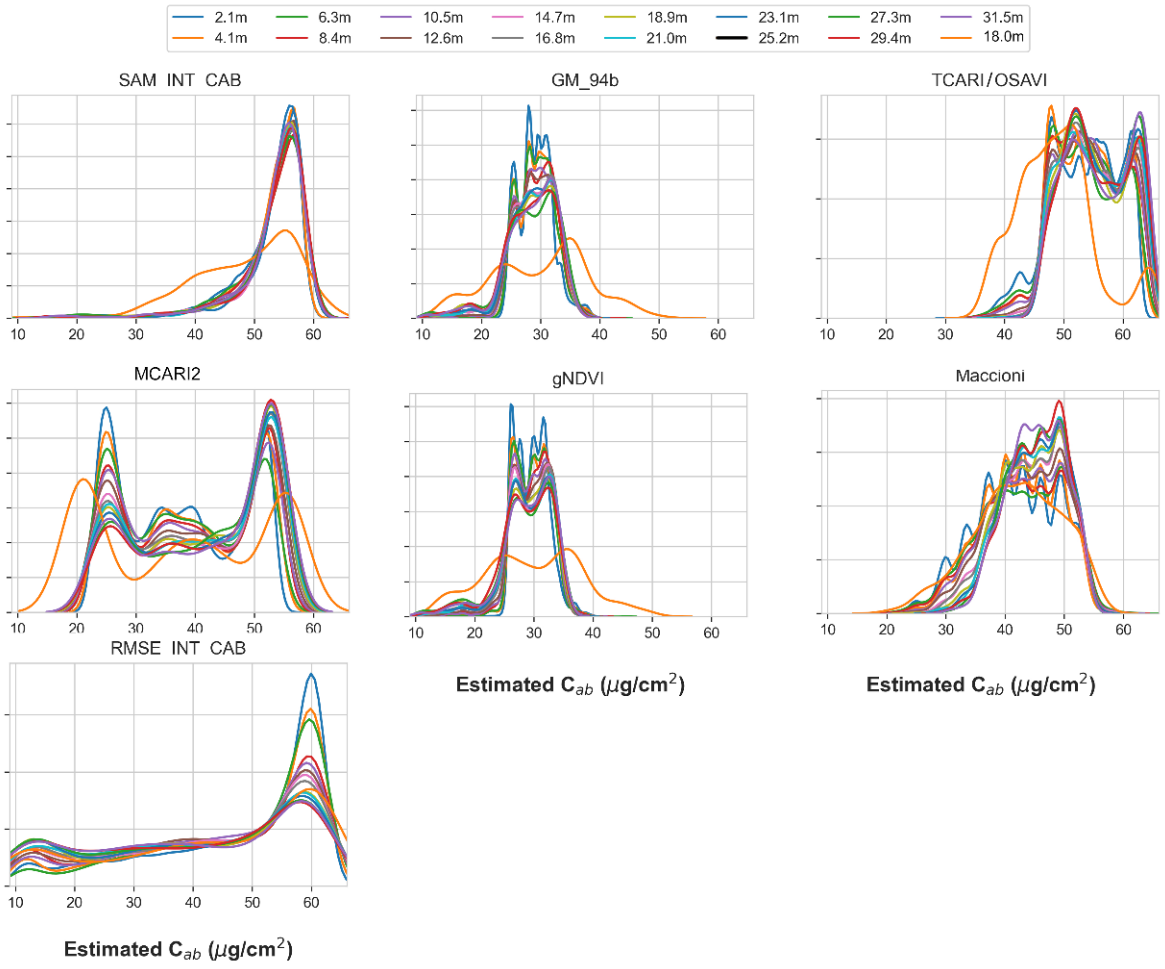


**Figure 5.2:** $C_{ab}$ inversion maps distributions. The separate orange curve is the distribution on the AV-C image

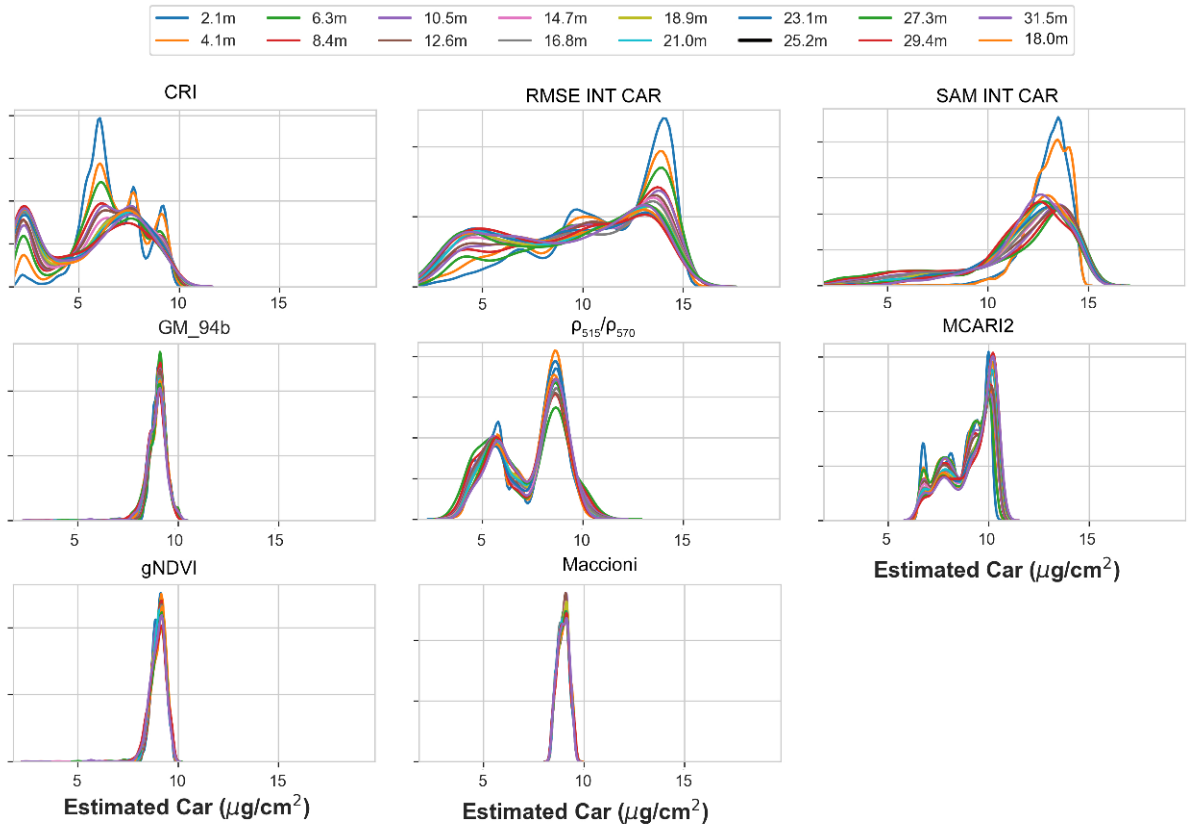


**Figure 5.3:** $C_{car}$ inversion maps distributions. The separate orange curve is the distribution on the AV-C image

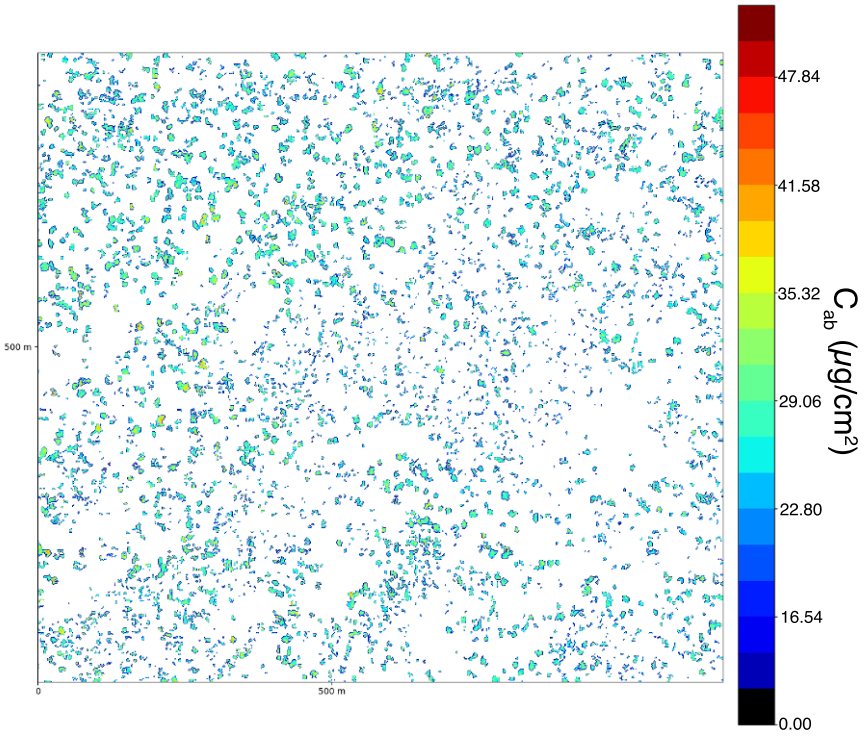


**(a)** $D_{GM_94b}$, $RMSE = 7.86 \mu g/cm^2$

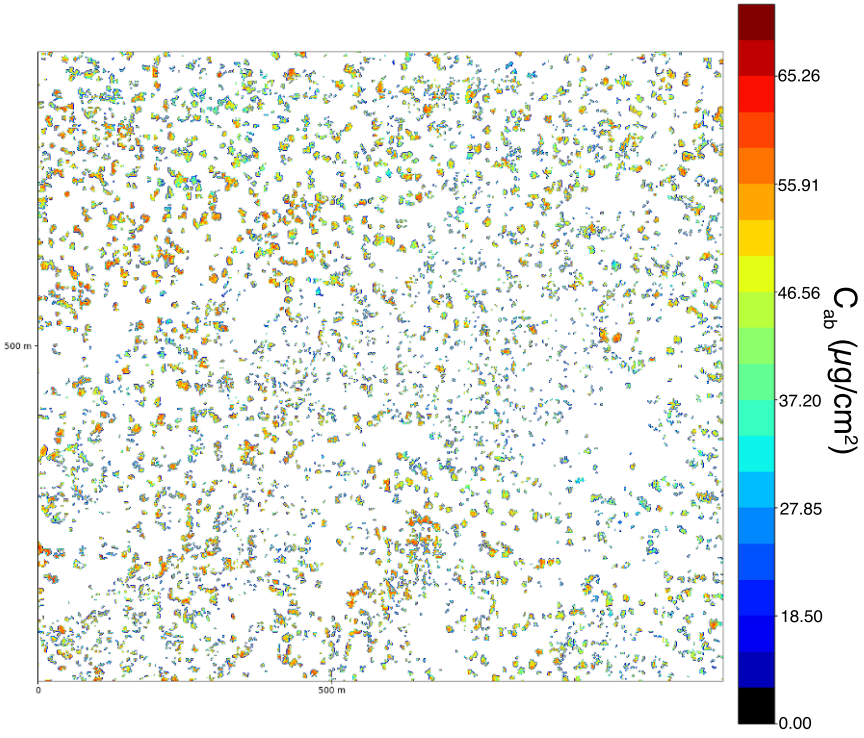


**(b)** SAM INT CAB, $RMSE = 5.93 \mu g/cm^2$

**Figure 5.4:** $C_{ab}$ inversion map at 2.1 m using $D_{GM_94b}$ and SAM INT CAB

## 5.3 DART parameters and convenience of the different LUTs for the inversion

Two classes of ground were considered for the DART simulation, senescent grass and a mixture of ground types as shown on Figure 4.2. Both simulations were ran and inversions done with the help of LUTs generated. The estimates obtained with the senescent grass ground showed worse results than with the other class for all variables inverted. This could be explained by the location of the estimated trees on the study site that are on areas on which the ground was classified with the mixture of ground types class (Figures 4.2 and 4.4). This showed the impact of the soil on the simulation and the performances and it should not be neglected if future estimations were to be done that way.

Four other LUTs were also created, in addition of the two already generated, based on the tree centered one by selecting different parts of the tree crown (North-West, North-East, South-East and South-West) in the DART simulated image in order to look at the impact of shadow or direct light on the inversions as the crown of the tree is not exactly lit in the same way depending on the direction considered. All of these four LUTs performed poorly or barely as well as the two first considered and were dropped for the rest of the study. Figure 5.5 shows how the pixels for the different LUTs were selected.

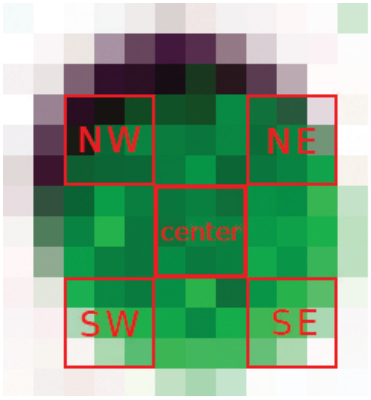


**Figure 5.5:** Pixel selection on a simulated tree for the different LUTs considered

Evaluating the impact of different LUTs is not easy as they show similar overall performance for $C_{ab}$ estimates. It seems that the primary objective of improving performance at spatial resolutions close to 2.1 m has been achieved for $gNDVI$ and $GM_94B$ with the tree centered pixels LUT in particular for the resolution 8.4 m. Surprisingly these two strategies continued to have better results in terms of RMSE up to the 31 m resolution but with a very low $R^2$. Concerning the estimation of carotenoids the tree centered pixels LUT does not seem to have brought better performances except for $\rho_{515}/\rho_{570}$. Only the standard LUT presented conclusive results for the inversion of the LAI, which could be

explained by the low LAI of the study site and therefore the need to have soil information in the LUT spectra.

## 5.4 HYPXIM (8 m) and SBG (30 m) spatial resolutions performances

Both of the HYPXIM and SBG instrument spatial resolutions showed similar performance in terms of RMSE. For $C_{ab}$ $gNDVI$ and $GM_94b$ had slightly better RMSEs at 8.4m than 31.5 m with similar $R^2$ ($RMSE_{gNDVI}$ = 8.24 µg/cm$^2$, $RMSE_{GM_94b}$ = 7.25 µg/cm$^2$ at 8.4m and $RMSE_{gNDVI}$ = 10.19 µg/cm$^2$, $RMSE_{GM_94b}$ = 10.69 µg/cm$^2$ at 31.5m). The difference $D_{\rho_{550}/\rho_{570}}$ and RMSE INT CAR methods performed better at 31.5 m but $R^2$ coefficients were very low at this resolution ($RMSE_{RMSE\ INT\ CAR}$ = 5.37 µg/cm$^2$, $RMSE_{\rho_{550}/\rho_{570}}$ = 3.41 µg/cm$^2$ at 8.4m and $RMSE_{RMSE\ INT\ CAR}$ = 3.00 µg/cm$^2$, $RMSE_{\rho_{550}/\rho_{570}}$ = 2.37 µg/cm$^2$ at 31.5m). All four methods used to estimate LAI showed better performances at 8.4 m. These criteria shows the possibility of estimating the biophysical properties and leaf pigments at these spatial resolutions with acceptable performances.

# Conclusion and prospects

The final goals of this internship were twofolds. On the one hand to confirm the results of Thomas Miraglio's work on the TONZI site [2, 3] on another woodland savanna site, SJER, with the same Mediterranean climate and the same distribution of species for summer 2014. On the other hand to evaluate the performance of the estimation of leaf pigments and biophysical properties using LUT based inversion methods at other spatial resolutions in particular 8 m and 30 m because they are those of the instruments of the future HYPXIM and SBG missions. Numerous inversion strategies were investigated, either using hyperspectral VIs or spectral intervals. Different LUTs were tested to assess the influence of soil on estimation performances. LAI and $C_{ab}$ retrieval performance showed promising results for summer 2014, $C_{car}$ estimations presented less satisfying results than in previous works but coherent behavior across spatial resolutions.

This study found multiple best inversion criteria, for LAI using RMSE between the pixels and the LUT over the 0.8 µm - 2.5 µm spectral range have provided the best results and steady $R^2$ coefficients over all the spatial resolutions. $C_{ab}$ showed best results when inverted with the tree centered pixels LUT using $D_{gNDVI}$ and $D_{GM_}94b$. $D_{\rho_{515}/\rho_{570}}$ presented the best accuracy overall but below Miraglio's studies and RMSE method performed poorly.

These results support the conclusions of the methodology developed by Miraglio and show the possibility of estimating the biophysical properties and leaf pigments at different spatial resolutions from 2 m to 30 m with acceptable performances using a simplified 3D RT model of the canopy of woodland savannas. These results should be extended to different dates to carry out seasonal monitoring and confirm the conclusion of this study. Estimation strategies of leaf water content and leaf mass per area should be further investigated to verify if promising results can be obtained for different dates.

Another way to investigate the estimation of these properties is the use of hybrid methods based on machine learning, including deep learning with the use of artificial neural networks with several layers. This method is proposed in future work aimed at completing the work of this study.

# Bibliography


[1] Susan Ustin and al. "Multiyear Multiseasonal Changes in Leaf and Canopy Traits Measured by AVIRIS over Ecosystems with Different Functional Type Characteristics Through the Progressive California Drought 2013-2015". In: *AGU Fall meeting*. 2015.

[2] Thomas Miraglio et al. "Monitoring LAI, Chlorophylls, and Carotenoids Content of a Woodland Savanna Using Hyperspectral Imagery and 3D Radiative Transfer Modeling". In: *Remote Sensing* 12.1 (2019), p. 28. DOI: 10.3390/rs12010028.

[3] Thomas Miraglio et al. "Correction: Miraglio, Thomas, et al. Monitoring LAI, Chlorophylls, and Carotenoids Content of a Woodland Savanna Using Hyperspectral Imagery and 3D Radiative Transfer Modeling". In: *Remote Sensing* 12.14 (2020), p. 2263. DOI: 10.3390/rs12142263.

[4] *Rapport annuel ONERA 2019*. Tech. rep. 2020, pp. 16–17. URL: https://www.onera.fr/sites/default/files/ressources_documentaires/ONERA-Rapport-Annuel-2019.pdf.

[5] J. M. O. Scurlock, G. P. Asner, and S. T. Gower. "Worldwide Historical Estimates of Leaf Area Index, 1932-2000". In: (2002). DOI: 10.2172/814100.

[6] Jean-Philippe Gastellu-Etchegorry. "Modeling radiative transfer in heterogeneous 3-D vegetation canopies". In: *Remote Sensing of Environment* 58.2 (1996), pp. 131–156. DOI: 10.1016/0034-4257(95)00253-7.

[7] Karine Adeline and al. "The Role of Species, Structure, and Biochemical Traits in the Spatial Distribution of a Woodland Community". In: *AGU Fall meeting*. 2015.

[8] Anna Jakomulska, Bogdan Zagajewski, and Anna Traut. "Application of Field Remote Sensing Techniques for Vegetation Investigation. Case Study of Siwica Glade Reserve". In: *Miscellanea Geographica* 10.1 (2002), pp. 279–306. DOI: 10.2478/mgrsd-2002-0032.

[9] Robert O Green et al. "Imaging Spectroscopy and the Airborne Visible/Infrared Imaging Spectrometer (AVIRIS)". In: *Remote Sensing of Environment* 65.3 (1998), pp. 227–248. DOI: 10.1016/s0034-4257(98)00064-9.

[10] Hartmut K. Lichtenthaler. "[34] Chlorophylls and carotenoids: Pigments of photosynthetic biomembranes". In: *Methods in Enzymology Plant Cell Membranes* (1987), pp. 350–382. DOI: 10.1016/0076-6879(87)48036-1.

[11] Hartmut K. Lichtenthaler and Claus Buschmann. "Chlorophylls and Carotenoids: Measurement and Characterization by UV-VIS Spectroscopy". In: *Current Protocols in Food Analytical Chemistry* 1.1 (2001). DOI: 10.1002/0471142913.faf0403s01.

[12] Hongliang Fang et al. "An Overview of Global Leaf Area Index (LAI): Methods, Products, Validation, and Applications". In: *Reviews of Geophysics* 57.3 (2019), pp. 739–799. DOI: 10.1029/2018rg000608.

[13] Xavier Briottet et al. "HYPXIM: A new hyperspectral sensor combining science/defence applications". In: *2011 3rd Workshop on Hyperspectral Image and Signal Processing: Evolution in Remote Sensing (WHISPERS)* (2011). DOI: 10.1109/whispers.2011.6080957.

[14] C. Miesch et al. "Direct and inverse radiative transfer solutions for visible and near-infrared hyperspectral imagery". In: *IEEE Transactions on Geoscience and Remote Sensing* 43.7 (2005), pp. 1552–1562. DOI: 10.1109/tgrs.2005.847793.

[15] D Haboudane. "Hyperspectral vegetation indices and novel algorithms for predicting green LAI of crop canopies: Modeling and validation in the context of precision agriculture". In: *Remote Sensing of Environment* 90.3 (2004), pp. 337–352. DOI: 10.1016/j.rse.2003.12.013.

[16] Schölkopf Bernhard and Alexander J. Smola. *Learning with kernels: support vector machines, regularization, optimization, and beyond*. MIT Press, 2002. DOI: 10.7551/mitpress/4175.001.0001.

[17] J.p. Gastellu-Etchegorry, F. Gascon, and P. Estève. "An interpolation procedure for generalizing a look-up table inversion method". In: *Remote Sensing of Environment* 87.1 (2003), pp. 55–71. DOI: 10.1016/s0034-4257(03)00146-9.

[18] F. Gascon et al. "Retrieval of forest biophysical variables by inverting a 3-D radiative transfer model and using high and very high resolution imagery". In: *International Journal of Remote Sensing* 25.24 (2004), pp. 5601–5616. DOI: 10.1080/01431160412331291305.

[19] Jean-Baptiste Feret et al. "PROSPECT-4 and 5: Advances in the leaf optical properties model separating photosynthetic pigments". In: *Remote Sensing of Environment* 112.6 (2008), pp. 3030–3043. DOI: 10.1016/j.rse.2008.02.012.

[20] Marie Weiss et al. "Investigation of a model inversion technique to estimate canopy biophysical variables from spectral and directional reflectance data". In: *Agronomie* 20.1 (2000), pp. 3–22. DOI: 10.1051/agro:2000105.

[21] Andrea Maccioni, Giovanni Agati, and Piero Mazzinghi. "New vegetation indices for remote measurement of chlorophylls based on leaf directional reflectance spectra". In: *Journal of Photochemistry and Photobiology B: Biology* 61.1-2 (2001), pp. 52–61. DOI: 10.1016/s1011-1344(01)00145-2.

[22] Rcg Smith et al. "Forecasting wheat yield in a Mediterranean-type environment from the NOAA satellite". In: *Australian Journal of Agricultural Research* 46.1 (1995), p. 113. DOI: 10.1071/ar9950113.

[23] Anatoly Gitelson and Mark N. Merzlyak. "Spectral Reflectance Changes Associated with Autumn Senescence of Aesculus hippocastanum L. and Acer platanoides L. Leaves. Spectral Features and Relation to Chlorophyll Estimation". In: *Journal of Plant Physiology* 143.3 (1994), pp. 286–292. DOI: 10.1016/s0176-1617(11)81633-0.

[24] Driss Haboudane et al. "Integrated narrow-band vegetation indices for prediction of crop chlorophyll content for application to precision agriculture". In: *Remote Sensing of Environment* 81.2-3 (2002), pp. 416–426. DOI: 10.1016/s0034-4257(02)00018-4.

[25] Rocío Hernández-Clemente, Rafael M. Navarro-Cerrillo, and Pablo J. Zarco-Tejada. "Carotenoid content estimation in a heterogeneous conifer forest using narrow-band indices and PROSPECT DART simulations". In: *Remote Sensing of Environment* 127 (2012), pp. 298–315. DOI: 10.1016/j.rse.2012.09.014.

[26] Anatoly A. Gitelson et al. "Relationship between gross primary production and chlorophyll content in crops: Implications for the synoptic monitoring of vegetation productivity". In: *Journal of Geophysical Research* 111.D8 (2006). DOI: 10.1029/2005jd006017.

[27] Compton J. Tucker. "Red and photographic infrared linear combinations for monitoring vegetation". In: *Remote Sensing of Environment* 8.2 (1979), pp. 127–150. DOI: 10.1016/0034-4257(79)90013-0.

[28] J. Qi et al. "A modified soil adjusted vegetation index". In: *Remote Sensing of Environment* 48.2 (1994), pp. 119–126. DOI: 10.1016/0034-4257(94)90134-1.

[29] P.j. Zarco-Tejada and S.l. Ustin. "Modeling canopy water content for carbon estimates from MODIS data at land EOS validation sites". In: *IGARSS 2001. Scanning the Present and Resolving the Future. Proceedings. IEEE 2001 International Geoscience and Remote Sensing Symposium (Cat. No.01CH37217)* (). DOI: 10.1109/igarss.2001.976152.

[30] R.E. Hunt and R.N Rock. "Detection of changes in leaf water content using Near- and Middle-Infrared reflectances". In: *Remote Sensing of Environment* 30 (1989), pp. 43–54. DOI: 10.1016/0034-4257(89)90046-1.

[31] L. Serrano, J. Peñuelas, and S.L Ustin. "Remote sensing of nitrogen and lignin in Mediterranean vegetation from AVIRIS data: Decomposing biochemical from structural signals". In: *Remote Sensing of Environment* 30 (1989), pp. 43–54. DOI: 10.1016/S0034-4257(02)00011-1.

[32] P.j Zarco-Tejada, C.a Rueda, and S.l Ustin. "Water content estimation in vegetation with MODIS reflectance data and model inversion methods". In: *Remote Sensing of Environment* 85.1 (2003), pp. 109–124. DOI: 10.1016/s0034-4257(02)00197-9.

# Appendices

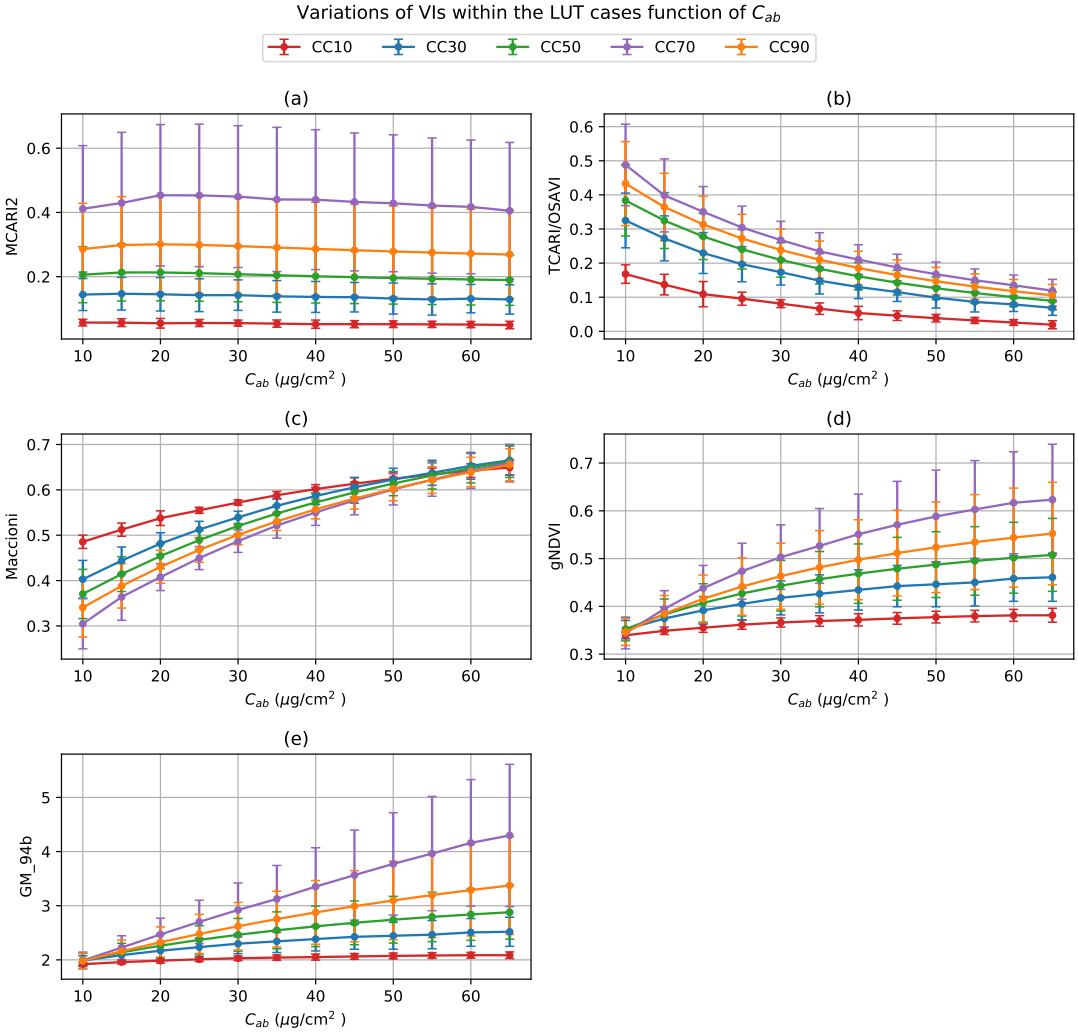


**Figure A.1:** VIs variation function of $C_{ab}$

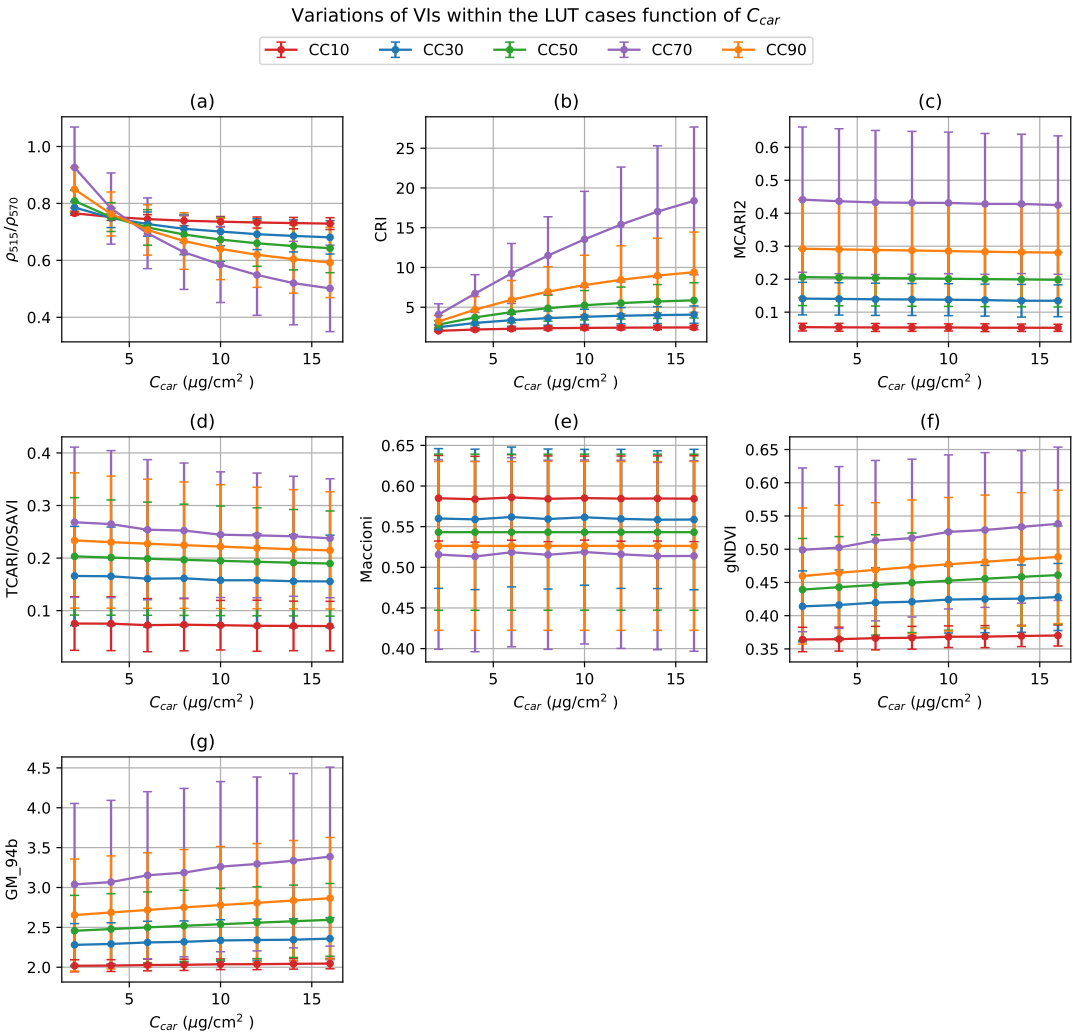


**Figure A.2:** VIs variation function of $C_{car}$

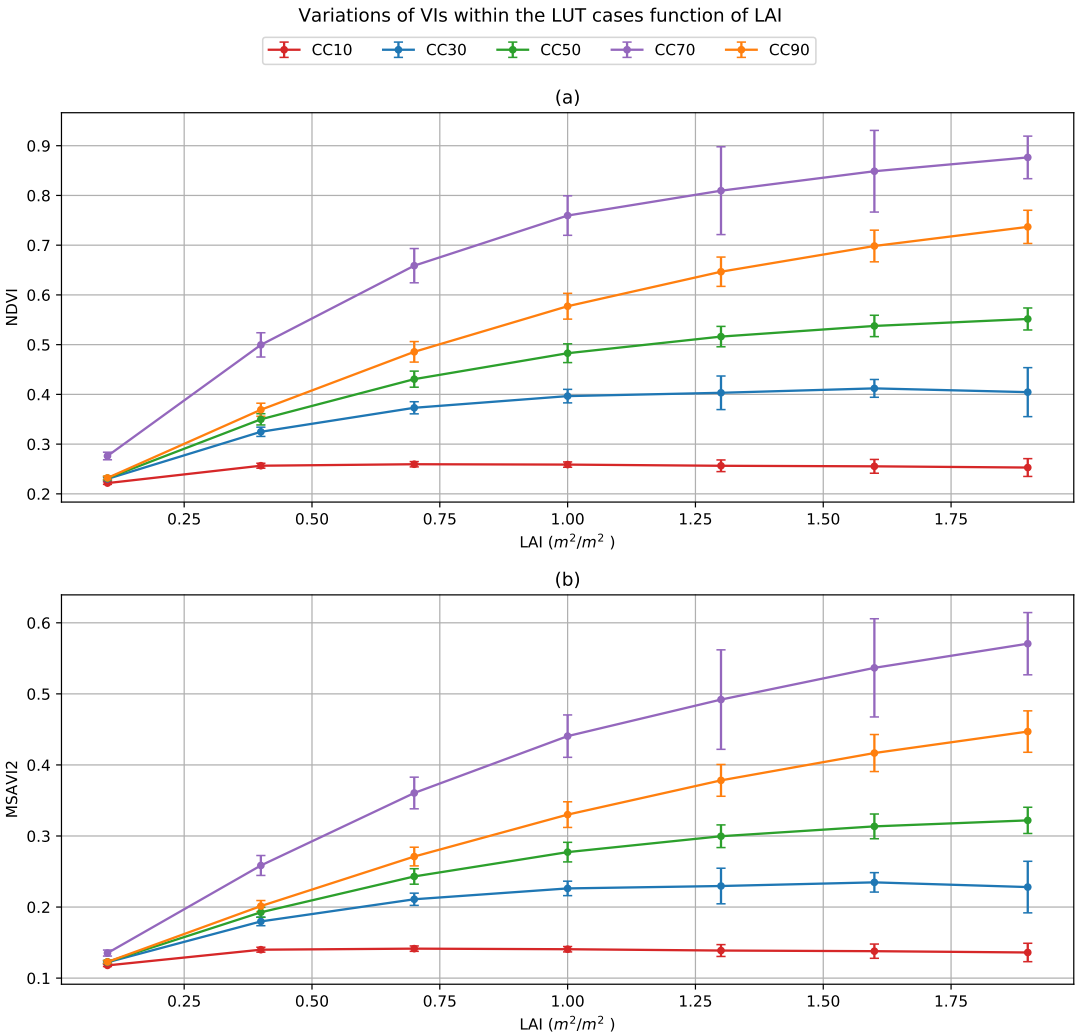


**Figure A.3:** VIs variation function of LAI

| Method | Spatial resolution (m) RMSE | | | | | | | | | | | | | | |
|---|---|---|---|---|---|---|---|---|---|---|---|---|---|---|---|
| $C_{ab}$ | 2.1 m | 4.2 m | 6.3 m | 8.4 m | 10.5 m | 12.6 m | 14.7 m | 16.8 m | 18.9 m | 21.0 m | 23.1 m | 25.2 m | 27.3 m | 29.4 m | 31.5 m |
| SAM INT CAB | 5.93 | 14.34 | 16.84 | 20.23 | 17.78 | 19.04 | 16.77 | 20.26 | 20.96 | 18.76 | 16.59 | 16.61 | 21.38 | 17.97 | 21.79 |
| $D_{MCARI2}$ | 6.92 | 13.75 | 9.48 | 15.36 | 16.41 | 13.09 | 9.76 | 12.08 | 14.83 | 8.09 | 15.10 | 9.35 | 9.16 | 10.46 | 16.47 |
| $D_{GM_94b}$ | 7.86 | 8.65 | 6.39 | 15.08 | 11.96 | 12.46 | 9.77 | 13.06 | 15.41 | 11.85 | 12.90 | 9.07 | 14.74 | 15.27 | 10.69 |
| $D_{gNDVI}$ | 8.42 | 8.54 | 5.07 | 13.53 | 5.05 | 9.83 | 11.58 | 12.57 | 14.97 | 11.68 | 13.29 | 8.61 | 15.51 | 10.39 | 10.19 |
| $D_{Macionni}$ | 8.73 | 7.72 | 11.70 | 15.19 | 10.95 | 10.91 | 12.19 | 10.74 | 10.50 | 10.26 | 9.28 | 10.31 | 11.75 | 13.63 | 11.87 |
| $D_{TCARI/OSAVI}$ | 10.10 | 16.81 | 15.41 | 18.59 | 15.05 | 19.42 | 18.71 | 21.17 | 18.96 | 20.74 | 15.86 | 17.57 | 14.17 | 17.42 | 15.68 |
| RMSE INT CAB | 21.19 | 19.20 | 17.54 | 18.93 | 27.67 | 21.95 | 20.85 | 23.54 | 23.61 | 24.77 | 18.12 | 18.89 | 22.95 | 24.45 | 19.67 |
| $C_{car}$ | 2.1 m | 4.2 m | 6.3 m | 8.4 m | 10.5 m | 12.6 m | 14.7 m | 16.8 m | 18.9 m | 21.0 m | 23.1 m | 25.2 m | 27.3 m | 29.4 m | 31.5 m |
| $D_{gNDVI}$ | 1.33 | 1.50 | 1.33 | 1.52 | 1.27 | 1.62 | 1.41 | 1.53 | 1.60 | 1.35 | 1.55 | 1.61 | 1.22 | 1.43 | 1.62 |
| $D_{Macionni}$ | 1.41 | 1.48 | 1.39 | 1.30 | 1.34 | 1.52 | 1.35 | 1.24 | 1.40 | 1.27 | 1.37 | 1.24 | 1.20 | 1.40 | 1.28 |
| $D_{MCARI2}$ | 1.45 | 2.48 | 1.60 | 1.47 | 1.32 | 1.40 | 1.62 | 1.56 | 1.90 | 1.61 | 2.29 | 1.20 | 1.44 | 1.34 | 1.71 |
| $D_{GM_94b}$ | 1.53 | 1.45 | 1.39 | 1.29 | 1.40 | 1.49 | 1.47 | 1.49 | 1.65 | 1.59 | 1.71 | 1.15 | 1.60 | 1.57 | 1.32 |
| $D_{CRI}$ | 1.82 | 3.95 | 4.29 | 4.73 | 4.18 | 2.53 | 2.88 | 2.51 | 4.75 | 4.70 | 2.48 | 4.30 | 4.06 | 4.71 | 4.74 |
| $D_{TCARI/OSAVI}$ | 2.63 | 1.61 | 1.67 | 1.36 | 1.07 | 1.14 | 2.07 | 1.18 | 1.05 | 1.72 | 1.89 | 1.38 | 1.33 | 1.58 | 1.39 |
| $D_{\rho_{515}/\rho_{570}}$ | 4.49 | 5.05 | 4.10 | 3.89 | 3.33 | 2.12 | 2.15 | 2.56 | 3.84 | 5.00 | 3.03 | 2.83 | 2.62 | 2.81 | 2.93 |
| RMSE INT CAR | 5.32 | 4.93 | 2.92 | 5.83 | 5.28 | 3.62 | 3.78 | 5.56 | 4.39 | 4.13 | 3.37 | 3.59 | 4.37 | 4.20 | 3.00 |
| SAM INT CAR | 5.42 | 5.39 | 3.60 | 5.64 | 5.72 | 4.24 | 5.14 | 4.60 | 4.13 | 6.24 | 4.16 | 5.42 | 4.79 | 5.74 | 4.73 |
| $C_w$ | 2.1 m | 4.2 m | 6.3 m | 8.4 m | 10.5 m | 12.6 m | 14.7 m | 16.8 m | 18.9 m | 21.0 m | 23.1 m | 25.2 m | 27.3 m | 29.4 m | 31.5 m |
| $D_{NDI7}$ | 0.0029 | 0.0021 | 0.0022 | 0.0034 | 0.0029 | 0.0031 | 0.0027 | 0.0029 | 0.0028 | 0.0027 | 0.0032 | 0.0028 | 0.0025 | 0.0024 | 0.0025 |
| $D_{SRWI}$ | 0.0032 | 0.0027 | 0.0020 | 0.0026 | 0.0027 | 0.0027 | 0.0021 | 0.0026 | 0.0034 | 0.0017 | 0.0017 | 0.0027 | 0.0026 | 0.0035 | 0.0032 |
| SAM INT EWT | 0.0031 | 0.0035 | 0.0036 | 0.0036 | 0.0038 | 0.0036 | 0.0030 | 0.0026 | 0.0025 | 0.0024 | 0.0023 | 0.0027 | 0.0027 | 0.0031 | 0.0023 |
| RMSE INT EWT | 0.0038 | 0.0042 | 0.0038 | 0.0038 | 0.0050 | 0.0032 | 0.0035 | 0.0019 | 0.0024 | 0.0015 | 0.0029 | 0.0027 | 0.0019 | 0.0021 | 0.0016 |
| $C_m$ | 2.1 m | 4.2 m | 6.3 m | 8.4 m | 10.5 m | 12.6 m | 14.7 m | 16.8 m | 18.9 m | 21.0 m | 23.1 m | 25.2 m | 27.3 m | 29.4 m | 31.5 m |
| RMSE INT LMA | 0.0030 | 0.0032 | 0.0060 | 0.0068 | 0.0050 | 0.0048 | 0.0042 | 0.0030 | 0.0029 | 0.0033 | 0.0030 | 0.0030 | 0.0063 | 0.0059 | 0.0056 |
| $D_{NDNI}$ | 0.0032 | 0.0035 | 0.0027 | 0.0033 | 0.0021 | 0.0038 | 0.0029 | 0.0032 | 0.0030 | 0.0026 | 0.0034 | 0.0028 | 0.0027 | 0.0038 | 0.0025 |
| $D_{NDLI}$ | 0.0018 | 0.0042 | 0.0036 | 0.0036 | 0.0047 | 0.0041 | 0.0034 | 0.0043 | 0.0042 | 0.0033 | 0.0043 | 0.0053 | 0.0039 | 0.0043 | 0.0048 |
| SAM INT LMA | 0.0020 | 0.0056 | 0.0049 | 0.0045 | 0.0057 | 0.0056 | 0.0058 | 0.0055 | 0.0060 | 0.0047 | 0.0058 | 0.0052 | 0.0051 | 0.0048 | 0.0054 |
| LAI | 2.1 m | 4.2 m | 6.3 m | 8.4 m | 10.5 m | 12.6 m | 14.7 m | 16.8 m | 18.9 m | 21.0 m | 23.1 m | 25.2 m | 27.3 m | 29.4 m | 31.5 m |
| RMSE INT LAI | 0.11 | 0.11 | 0.11 | 0.12 | 0.14 | 0.15 | 0.23 | 0.17 | 0.21 | 0.26 | 0.24 | 0.28 | 0.26 | 0.28 | 0.22 |
| SAM INT LAI | 0.26 | 0.27 | 0.28 | 0.29 | 0.31 | 0.30 | 0.30 | 0.30 | 0.28 | 0.38 | 0.29 | 0.37 | 0.33 | 0.33 | 0.52 |
| $D_{MSAVI2}$ | 0.27 | 0.28 | 0.28 | 0.30 | 0.28 | 0.35 | 0.37 | 0.35 | 0.35 | 0.38 | 0.39 | 0.42 | 0.43 | 0.42 | 0.43 |
| $D_{NDVI}$ | 0.30 | 0.29 | 0.27 | 0.26 | 0.24 | 0.30 | 0.28 | 0.28 | 0.26 | 0.25 | 0.27 | 0.31 | 0.32 | 0.33 | 0.27 |

**Table A.1:** Variable retrieval performances for the standard LUT results

| Method | Spatial resolution (m) RMSE | | | | | | | | | | | | | | |
|---|---|---|---|---|---|---|---|---|---|---|---|---|---|---|---|
| $C_{ab}$ | 2.1 m | 4.2 m | 6.3 m | 8.4 m | 10.5 m | 12.6 m | 14.7 m | 16.8 m | 18.9 m | 21.0 m | 23.1 m | 25.2 m | 27.3 m | 29.4 m | 31.5 m |
| $D_{GM_94b}$ | 6.38 | 9.58 | 7.89 | 7.25 | 9.38 | 9.98 | 9.98 | 10.30 | 8.79 | 9.40 | 8.21 | 6.62 | 6.55 | 12.22 | 10.02 |
| $D_{gNDVI}$ | 6.45 | 7.08 | 10.39 | 8.24 | 9.44 | 10.62 | 9.49 | 10.93 | 7.10 | 8.00 | 5.73 | 7.51 | 7.53 | 12.86 | 9.15 |
| $D_{MCARI2}$ | 8.68 | 9.81 | 14.35 | 14.39 | 9.26 | 13.61 | 6.37 | 14.63 | 14.12 | 11.89 | 10.66 | 5.82 | 12.71 | 10.33 | 13.02 |
| $D_{Macionni}$ | 9.92 | 6.29 | 12.16 | 14.43 | 11.43 | 11.94 | 13.43 | 12.91 | 12.32 | 12.61 | 11.97 | 12.13 | 13.45 | 15.93 | 13.98 |
| SAM INT CAB | 15.94 | 21.07 | 20.98 | 19.59 | 19.99 | 21.90 | 21.45 | 22.92 | 22.64 | 22.96 | 20.90 | 20.91 | 22.86 | 21.63 | 22.75 |
| $D_{TCARI/OSAVI}$ | 18.57 | 22.94 | 19.95 | 19.58 | 19.08 | 23.09 | 23.51 | 25.19 | 24.83 | 25.30 | 19.13 | 24.29 | 25.37 | 24.50 | 24.10 |
| RMSE INT CAB | 20.24 | 17.94 | 18.26 | 14.67 | 21.67 | 24.12 | 21.10 | 22.11 | 21.21 | 22.56 | 22.39 | 25.25 | 23.51 | 26.64 | 23.71 |
| $C_{car}$ | 2.1 m | 4.2 m | 6.3 m | 8.4 m | 10.5 m | 12.6 m | 14.7 m | 16.8 m | 18.9 m | 21.0 m | 23.1 m | 25.2 m | 27.3 m | 29.4 m | 31.5 m |
| $D_{TCARI/OSAVI}$ | 1.03 | 1.45 | 1.61 | 1.54 | 1.68 | 1.45 | 2.54 | 1.44 | 1.28 | 1.55 | 1.25 | 1.27 | 1.26 | 2.16 | 1.55 |
| $D_{gNDVI}$ | 1.45 | 1.37 | 1.60 | 1.41 | 1.33 | 1.28 | 1.23 | 1.31 | 1.52 | 1.33 | 1.22 | 1.41 | 1.55 | 1.34 | 1.55 |
| $D_{Macionni}$ | 1.46 | 1.37 | 1.35 | 1.38 | 1.40 | 1.28 | 1.46 | 1.41 | 1.48 | 1.23 | 1.28 | 1.35 | 1.51 | 1.25 | 1.40 |
| $D_{GM_94b}$ | 1.51 | 1.25 | 1.40 | 1.53 | 1.23 | 1.32 | 1.47 | 1.40 | 1.25 | 1.31 | 1.31 | 1.37 | 1.26 | 1.45 | 1.28 |
| $D_{MCARI2}$ | 1.62 | 1.14 | 1.95 | 1.95 | 1.44 | 1.29 | 1.22 | 1.24 | 1.69 | 1.61 | 1.11 | 0.84 | 1.51 | 1.02 | 1.51 |
| $D_{CRI}$ | 3.67 | 4.45 | 4.34 | 4.89 | 4.08 | 4.99 | 4.07 | 4.46 | 5.10 | 4.98 | 2.03 | 4.08 | 4.81 | 4.97 | 4.66 |
| $D_{\rho_{515}/\rho_{570}}$ | 3.76 | 3.69 | 3.26 | 3.41 | 3.04 | 2.23 | 2.26 | 2.33 | 3.10 | 3.84 | 2.50 | 2.80 | 2.45 | 2.29 | 2.37 |
| RMSE INT CAR | 4.27 | 3.85 | 2.77 | 5.37 | 4.86 | 4.14 | 3.40 | 4.90 | 4.24 | 3.60 | 2.64 | 3.86 | 4.25 | 4.32 | 3.56 |
| SAM INT CAR | 4.71 | 5.00 | 3.95 | 5.66 | 5.59 | 3.62 | 4.38 | 4.90 | 5.20 | 5.18 | 4.65 | 5.23 | 5.28 | 5.47 | 4.54 |
| $C_w$ | 2.1 m | 4.2 m | 6.3 m | 8.4 m | 10.5 m | 12.6 m | 14.7 m | 16.8 m | 18.9 m | 21.0 m | 23.1 m | 25.2 m | 27.3 m | 29.4 m | 31.5 m |
| SAM INT EWT | 0.0031 | 0.0030 | 0.0042 | 0.0037 | 0.0035 | 0.0037 | 0.0043 | 0.0015 | 0.0020 | 0.0037 | 0.0023 | 0.0033 | 0.0037 | 0.0029 | 0.0018 |
| $D_{NDI7}$ | 0.0036 | 0.0038 | 0.0031 | 0.0037 | 0.0035 | 0.0040 | 0.0043 | 0.0035 | 0.0042 | 0.0033 | 0.0037 | 0.0022 | 0.0037 | 0.0046 | 0.0043 |
| RMSE INT EWT | 0.0045 | 0.0040 | 0.0025 | 0.0031 | 0.0038 | 0.0033 | 0.0024 | 0.0024 | 0.0031 | 0.0015 | 0.0018 | 0.0020 | 0.0019 | 0.0020 | 0.0021 |
| $D_{SRWI}$ | 0.0032 | 0.0042 | 0.0026 | 0.0022 | 0.0039 | 0.0025 | 0.0040 | 0.0027 | 0.0044 | 0.0026 | 0.0027 | 0.0041 | 0.0034 | 0.0034 | 0.0033 |
| $C_m$ | 2.1 m | 4.2 m | 6.3 m | 8.4 m | 10.5 m | 12.6 m | 14.7 m | 16.8 m | 18.9 m | 21.0 m | 23.1 m | 25.2 m | 27.3 m | 29.4 m | 31.5 m |
| $D_{NDNI}$ | 0.0031 | 0.0027 | 0.0029 | 0.0033 | 0.0023 | 0.0039 | 0.0026 | 0.0024 | 0.0027 | 0.0025 | 0.0034 | 0.0028 | 0.0029 | 0.0032 | 0.0020 |
| $D_{NDLI}$ | 0.0036 | 0.0037 | 0.0029 | 0.0041 | 0.0047 | 0.0040 | 0.0034 | 0.0043 | 0.0033 | 0.0029 | 0.0043 | 0.0042 | 0.0035 | 0.0041 | 0.0037 |
| SAM INT LMA | 0.0041 | 0.0045 | 0.0026 | 0.0045 | 0.0045 | 0.0048 | 0.0028 | 0.0047 | 0.0030 | 0.0045 | 0.0047 | 0.0037 | 0.0034 | 0.0037 | 0.0043 |
| RMSE INT LMA | 0.0046 | 0.0051 | 0.0058 | 0.0065 | 0.0055 | 0.0049 | 0.0025 | 0.0048 | 0.0029 | 0.0022 | 0.0039 | 0.0028 | 0.0050 | 0.0055 | 0.0050 |
| LAI | 2.1 m | 4.2 m | 6.3 m | 8.4 m | 10.5 m | 12.6 m | 14.7 m | 16.8 m | 18.9 m | 21.0 m | 23.1 m | 25.2 m | 27.3 m | 29.4 m | 31.5 m |
| SAM INT LAI | 0.22 | 0.23 | 0.24 | 0.23 | 0.24 | 0.24 | 0.26 | 0.25 | 0.25 | 0.25 | 0.28 | 0.28 | 0.29 | 0.29 | 0.26 |
| RMSE INT LAI | 0.24 | 0.26 | 0.28 | 0.29 | 0.30 | 0.32 | 0.35 | 0.34 | 0.36 | 0.37 | 0.39 | 0.38 | 0.40 | 0.41 | 0.37 |
| $D_{NDVI}$ | 0.47 | 0.48 | 0.50 | 0.50 | 0.50 | 0.52 | 0.54 | 0.54 | 0.54 | 0.54 | 0.55 | 0.57 | 0.58 | 0.58 | 0.57 |
| $D_{MSAVI2}$ | 0.52 | 0.53 | 0.53 | 0.54 | 0.54 | 0.56 | 0.57 | 0.56 | 0.58 | 0.59 | 0.59 | 0.60 | 0.61 | 0.61 | 0.61 |

**Table A.2:** Variable retrieval performances for the tree centered pixels LUT

**Abstract** — In recent decades, ecologists have defined essential biodiversity variables (EBVs) to describe the steep decline of the vegetation biodiversity. These are relevant indicators of plant's health and functioning, such as leaf pigment contents (chlorophylls a and b content ($C_{ab}$) or carotenoid content ($C_{car}$) and the leaf area index (LAI), that can be estimated through hyperspectral imagery. Their measurement on a seasonal and yearly basis is critical to monitor plant response and adaptation to stress, such as droughts. While extensively done over dense canopies, estimation of these variables over tree-grass ecosystems with very low overstory LAI (mean site LAI $< 1$ m$^2$/m$^2$), such as woodland savannas, is lacking. We investigated the use of look-up table (LUT)-based inversion of a radiative transfer model to retrieve LAI and leaf $C_{ab}$ and $C_{car}$ from AVIRIS images at spatial resolutions ranging from 2 m to 30 m at a single date over a broadleaved woodland savanna during the California drought. We compared the performances of different cost functions in the inversion step. We demonstrated the spatial consistency of our LAI, $C_{ab}$, and $C_{car}$ estimations using validation data from low and high canopy cover parts of the site. We concluded that LUT-based inversions of hyperspectral images, achieved with a simple geometric representation of the canopy within a 3D radiative transfer model (RTM), are a valid means of monitoring woodland savannas and more generally sparse forests, although for maximum applicability, the inversion cost functions should be selected using validation data from multiple dates. Validation revealed that for monitoring use: The root mean square error (RMSE) between the pixels reflectances and simulated from the RTM outperformed other indices for LAI estimations (RMSE = 0.15 m$^2$/m$^2$ in average, $R^2 = 0.70$); the band ratios $\frac{\rho_{0.750\mu m}}{\rho_{0.550\mu m}}$ (gNDVI) and $\frac{\rho_{0.780\mu m} - \rho_{0.550\mu m}}{\rho_{0.780\mu m} + \rho_{0.550\mu m}}$ (GM_94b) retrieved $C_{ab}$ more accurately than other chlorophylls indices (RMSE = 6.45 µg/cm$^2$ for gNDVI and RMSE = 6.38 µg/cm$^2$ for GM_94b); RMSE over the 0.5–0.55 µm interval showed promising results for $C_{car}$ estimations.

**Keywords:** Remote Sensing; DART; AVIRIS; leaf pigments; Mediterranean forest;

ISAE
10, avenue Édouard Belin
BP 54032
31055 Toulouse CEDEX 4